Tests of General Relativity with the Stochastic Gravitational-Wave Background

Thomas Callister,[1,*] Sylvia Biscoveanu,[2] Nelson Christensen,[3,4] Maximiliano Isi,[1] Andrew Matas,[5] Olivier Minazzoli,[6,4] Tania Regimbau,[4] Mairi Sakellariadou,[7] Jay Tasson,[3] and Eric Thrane[8,9]

[1]*LIGO Laboratory, California Institute of Technology, Pasadena, CA 91125, USA*
[2]*The Pennsylvania State University, University Park, PA 16802, USA*
[3]*Carleton College, Northfield, MN 55057, USA*
[4]*Artemis, Université Côte d'Azur, Observatoire Côte d'Azur, CNRS, CS 34229, F-06304 Nice Cedex 4, France*
[5]*University of Minnesota, Minneapolis, MN 55455, USA*
[6]*Centre Scientifique de Monaco, 8 Quai Antoine 1er, MC 98000, Monaco*
[7]*King's College London, University of London, Strand, London WC2R 2LS, UK*
[8]*School of Physics and Astronomy, Monash University, Clayton, Victoria 3800, Australia*
[9]*OzGrav: The ARC Centre of Excellence for Gravitational-Wave Discovery, Hawthorn, Victoria 3122, Australia*

(Dated: April 28, 2017)

The direct observation of gravitational waves with Advanced LIGO offers novel opportunities to test general relativity in strong-field, highly dynamical regimes. One such opportunity is the measurement of gravitational-wave polarizations. While general relativity predicts only two tensor gravitational-wave polarizations, general metric theories of gravity allow for up to four additional vector and scalar modes. The detection of these alternative polarizations would represent a clear violation of general relativity. However, the current generation of ground-based detectors is unable to sensitively determine the polarization content of transient gravitational-wave signals. Observation of the stochastic gravitational-wave background, in contrast, offers a means of directly measuring gravitational-wave polarizations. The stochastic background, arising from the superposition of many individually unresolvable gravitational-wave signals, may be detectable by Advanced LIGO at design-sensitivity. In this paper, we present a Bayesian method with which to detect and characterize the polarization of the stochastic background. We explore prospects for estimating parameters of the background, and quantify the limits that Advanced LIGO can place on vector and scalar polarizations in the absence of a detection. Finally, we investigate how the addition of future terrestrial detectors like Advanced Virgo will aid our ability to detect or constrain alternative polarizations in the stochastic background. We find that, although the addition of Advanced Virgo does not notably improve detection prospects, it may dramatically improve our ability to estimate the parameters of backgrounds of mixed polarization.

arXiv:1704.08373v1 [gr-qc] 26 Apr 2017

I. INTRODUCTION

The recent Advanced LIGO observations of the coalescing binary black holes GW150914, GW151226, and LVT151012 have initiated the era of gravitational-wave astronomy [1–4]. Beyond their role as astrophysical messengers, gravitational waves offer unique opportunities to test gravity in previously unexplored regimes [5–8]. The direct detection of gravitational waves has already enabled novel experimental checks on general relativity, placing the best model-independent dynamical bound to date on the graviton mass and limiting deviations of post-Newtonian coefficients from their predicted values [3, 9–11].

The measurement of gravitational-wave polarizations represents another avenue by which to test general relativity. While general relativity allows for the existence of only two gravitational-wave polarizations (the tensor plus and cross modes), general metric theories of gravity may allow for up to four additional polarizations: the x and y vector modes, and the breathing and longitudinal scalar modes [5, 6, 8]. The effects of all six polarizations on a ring of freely-falling test particles are shown in Fig. 1. The detection of these alternative polarization modes would represent a clear violation of general relativity, while their non-detection may serve to experimentally constrain extended theories of gravity.

When allowing for all six polarization modes, however, the two-detector Advanced LIGO network is unable to distinguish the polarization of transient gravitational-wave signals, like those from binary black holes [3, 7–9, 12]. A network of at least six detectors is generically required to uniquely determine the polarization content (possibly vector or scalar) of a gravitational-wave transient [7, 8, 13]. Additionally, the two LIGO detectors are nearly co-oriented, further decreasing LIGO's ability to distinguish among different polarizations [3, 8, 9]. Thus, despite Advanced LIGO's strong detection of at least two binary black hole mergers, we have no direct confirmation that the signals from these events are indeed the tensorial gravitational waves predicted by general relativity [3, 9].

Beyond the direct detection of binary coalescences, another target for current and future detectors is the observation of the astrophysical stochastic gravitational-wave background, formed via the superposition of all gravitational-wave sources that are too weak or too distant to individually resolve [12, 14–18]. Although the strength of the background remains highly uncertain, it may be detected by Advanced LIGO in as few as two years of coincident observation at design-sensitivity [18–20]. Unlike direct searches for binary black holes, Advanced LIGO searches for long-lived sources like the stochastic background and rotating neutron stars [12, 21–26] *are* currently capable of directly measuring gravitational-wave polarizations without the introduction of additional detectors. The obser-

* tcallist@caltech.edu

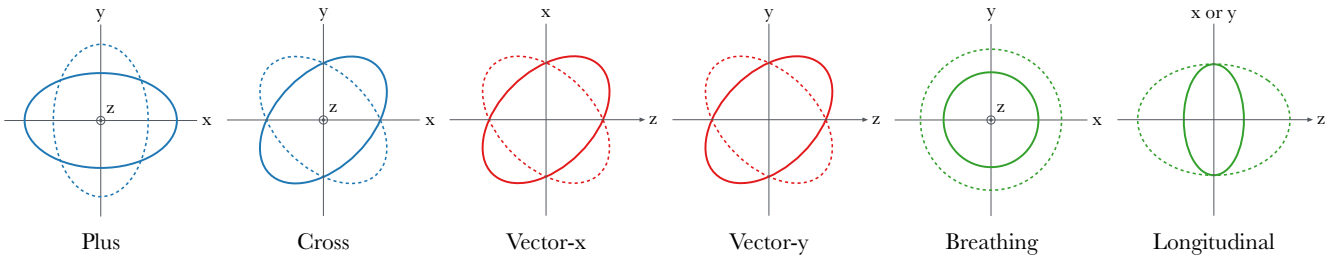

FIG. 1. Deformation of a ring of freely-falling test particles under the six gravitational wave polarizations allowed in general metric theories of gravity. Each wave is assumed to propagate in the z-direction (out of the page for the plus, cross, and breathing modes; to the right for the vector-x, vector-y, and longitudinal modes). While general relativity allows only for two tensor polarizations (plus and cross), alternate theories allow for two vector (x and y) and/or two scalar (breathing and longitudinal) polarization modes.

vation of the stochastic background would therefore enable novel checks on general relativity not possible with transient searches using the current generation of gravitational-wave detectors.

In this paper, we explore the means by which Advanced LIGO can detect and identify alternative polarizations in the stochastic background. First, in Sect. II, we consider possible theorized sources which might produce a background of alternative polarizations. We note, though, that stochastic searches are largely unmodeled, requiring few assumptions about potential sources or theories giving rise to alternative polarization modes (see, however, Sect. VI).

In Sect. III we discuss the tools used for detecting the stochastic background and compare the efficacy of standard methods with those optimized for alternative polarizations. In Sect. IV we then propose a Bayesian method with which to both detect generically-polarized backgrounds and determine if alternative polarization modes are present. Next, in Sect. V we explore prospects for estimating the polarization content of the stochastic background. We quantify the limits that Advanced LIGO can place on the presence of alternative polarizations in the stochastic background, limits which may translated into constraints on specific alternative theories of gravity.

As new detectors are brought online in the coming years, searches for alternative polarizations in the stochastic background will become ever more sensitive. In both Sects. IV and V, we therefore investigate how the addition of Advanced Virgo improves our ability to detect or constrain backgrounds of alternative polarizations. Finally, in Sect. VI we ask if our proposed search is robust against unexpectedly complex backgrounds of standard tensor polarizations.

II. EXTENDED THEORIES OF GRAVITY AND ALTERNATIVE POLARIZATION MODES

Searches for the stochastic background are largely unmodeled, making minimal assumptions about the source of a measured background. Nevertheless, it is interesting to consider which sources might give rise to a detectable background of alternative polarization modes. In this section we briefly consider several possibilities that have been proposed in the literature. We will focus mainly on scalar-tensor theories, which predict both tensor and scalar-polarized gravitational waves [27]. Our discussion below is not meant to be exhaustive; there may well exist additional sources that can give rise to backgrounds of extra polarization modes. In particularly, we do not discuss possible sources of vector modes, predicted by various alternative theories of gravity (see Ref. [13] and references therein). Note that, while advanced detectors may not be sensitive to the sources described below, these sources may become increasingly relevant for third generation detectors (or beyond).

One potential source of scalar gravitational waves are core-collapse supernovae (CCSNe). Although spherically-symmetric stellar collapses do not radiate gravitational waves in general relativity, they do emit scalar breathing modes in canonical scalar-tensor theories. While the direct observation of gravitational waves from CCSNe is expected to place strong constraints on scalar-tensor theories [28], only supernovae within the Milky Way are likely to be directly detectable using current instruments [29, 30]. Such events are rare, occurring at a rate between $(0.6 - 10.5) \times 10^{-2}\,\mathrm{yr}^{-1}$ [31]. The stochastic gravitational-wave background, on the other hand, is dominated by distant undetected sources, and so in principle it is possible that a CCSNe background of breathing modes could be detected before the observation of a single Galactic supernova [32, 33]. However, realistic simulations of monopole emission from CCSNe predict only weak scalar emission [28]. Nevertheless, certain extreme phenomenological supernovae models predict gravitational radiation many orders of magnitude stronger than in more conventional models [29]. According to such models, CCSNe may contribute non-negligibly to the stochastic background.

Compact binary coalescences may also contribute to a stochastic background of scalar gravitational waves. In many scalar-tensor theories, bodies may carry a "scalar charge" that sources the emission of scalar gravitational waves [34, 35]. Monopole scalar radiation is suppressed due to conservation of scalar charge, but in a general scalar-tensor theory there is generally no conservation law suppressing dipole radiation. Scalar dipole radiation from compact binaries is enhanced by a factor of $(v/c)^{-2}$ relative to ordinary quadrupole tensor radiation (where v is the orbital velocity of the binary and c the

speed of light), and thus represents a potentially promising source of scalar gravitational waves. Electromagnetic observations of binary neutron stars place stringent constraints on anomalous energy loss beyond that predicted by general relativity; these constraints may be translated into a strong limit on the presence of additional scalar-dipole radiation [36, 37]. Such limits, though, are strongly model-dependent, assuming *a priori* only small deviations from general relativity. Additionally, pure vacuum solutions like binary black holes are not necessarily subject to these constraints. If, for example, the scalar field interacts with curvature only through a linear coupling to the Gauss-Bonnet term, scalar radiation is produced by binary black holes but not by binary neutron stars [38]. Alternatively, binary black holes can avoid the no-hair theorem and obtain a scalar charge if moving through a time-dependent or spatially-varying background scalar field [39, 40].

In Appendix E, we consider the possible contribution of binary black hole mergers to a scalar-polarized stochastic background and quantify the constraints Advanced LIGO may place on this background. We find that constraints on scalar-tensor theories derived from the stochastic background are likely not as strong as those placed by the direct observation of binary black hole mergers [38]. Nevertheless, since the stochastic background probes a distinct black hole population at redshifts beyond the range of direct detection, constraints on the scalar background may still be valuable. Stochastic constraints would prove important, for instance, if there exists a background scalar field which evolves in time.

A variety of exotic sources may generically contribute to stochastic backgrounds of alternative polarizations as well. Cosmic strings, for instance, generically radiate alternative polarizations in extended theories of gravity and may therefore contribute extra polarization modes to the stochastic gravitational-wave background [41, 42]. Another potential source of stochastic backgrounds of alternative polarizations are the so-called "bubble walls" generated by first order phase transitions in the early Universe [43–45]. In scalar-tensor theories, bubbles are expected to produce strong monopolar emission [34]. Gravitational waves from bubbles are heavily redshifted, though, and today may have frequencies too low for Advanced LIGO to detect [44]. Bubble walls may therefore be a more promising target for future space-based detectors like LISA than for current ground-based instruments.

Finally, we note that it is also possible for alternative polarizations to be generated more effectively from sources at very large distances. There are several ways in which this might occur. First, modifications to the gravitational-wave dispersion relation can lead to mixing between different polarizations in vacuum (an effect analogous to neutrino oscillations) [46, 47]. Thus alternative polarizations can be generated during propagation, even if only tensor modes are produced at the source. This effect would build with the distance to a given gravitational-wave source. Such behavior is among the effects arising from generic Lorentz-violating theories of gravity [48, 49]. While birefringence and dispersion of the standard plus and cross modes have been explored observationally in this context [49, 50], the phenomenological implications of additional polarization modes remains an open issue at present. Secondly, in many alternative theories fundamental constants (such as Newton's constant G) are elevated to dynamical fields; these fields may have behaved differently at earlier stages in the Universe's evolution [51, 52]. As a consequence, local constraints on scalar emission may not apply to emission from remote sources. Additionally, it is in principle possible for local sources to be affected by screening mechanisms that do not affect some remote sources [53].

III. STOCHASTIC BACKGROUNDS OF ALTERNATIVE POLARIZATIONS

Gravitational-wave backgrounds are conventionally described by their energy-density spectra [54]

$$\Omega(f) = \frac{1}{\rho_c}\frac{d\rho_{\rm GW}(f)}{d\ln f}, \tag{1}$$

defined as the fraction of the critical energy density $\rho_c = 3H_0^2c^2/(8\pi G)$ contained in gravitational waves per logarithmic frequency interval $d\ln f$. Here, H_0 is the Hubble constant and G is Newton's constant. When allowing for generic gravitational-wave polarizations, the total energy density of the stochastic background is the sum of energies in tensor, vector, and scalar polarizations:

$$\Omega(f) = \Omega^T(f) + \Omega^V(f) + \Omega^S(f). \tag{2}$$

We assume that the three polarization sectors are uncorrelated and that the tensor and vector sectors are individually unpolarized, with equal energy in the tensor plus and cross modes and equal energy in vector-x and vector-y modes. The scalar sector, meanwhile, is not necessarily unpolarized, since breathing and longitudinal modes cannot be rotated into one another. However, the LIGO detectors' responses to breathing and longitudinal modes are fully-degenerate, and so Advanced LIGO is sensitive only to the total energy $\Omega^S(f)$ in scalar modes and not to the individual energies in the breathing and longitudinal polarizations [8, 22].

The effect of the stochastic background is to introduce a weak, correlated signal into networks of gravitational-wave detectors. Searches for the stochastic background therefore measure the cross-correlation $\hat{Y}(f) \propto \tilde{s}_1^*(f)\tilde{s}_2(f)$ between the strain $\tilde{s}_1(f)$ and $\tilde{s}_2(f)$ measured by pairs of detectors (see Ref. [12] for a comprehensive review of stochastic background detection methods). Assuming that the background is isotropic, stationary, and Gaussian, the measured cross-correlation is related to the background's energy density by [12, 22, 54]

$$\langle\tilde{s}_1^*(f)\tilde{s}_2(f')\rangle = \frac{3H_0^2}{20\pi^2}\delta(f-f')|f|^{-3}\gamma_a(f)\Omega^a(f), \tag{3}$$

where repeated indices denote summation over tensor, vector, and scalar modes. The overlap reduction functions $\gamma_a(f)$ quantify the sensitivity of detector pairs to isotropic backgrounds of each polarization [55] (see Appendix A for details).

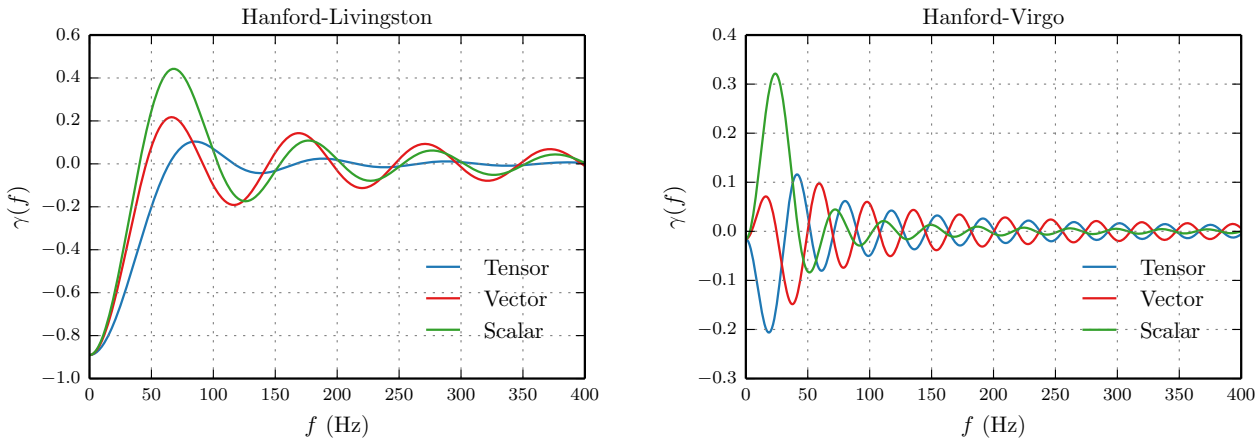

FIG. 2. Overlap reduction functions quantifying the sensitivities of the Hanford-Livingston (left) and Hanford-Virgo (right) baselines to isotropic backgrounds of tensor, vector, and scalar-polarized gravitational waves. The distance between Hanford and Virgo is much larger than that between Hanford and Livingston; the Hanford-Virgo overlap reduction functions are therefore smaller in amplitude and more rapidly oscillatory.

In the left side of Fig. 2, we show the overlap reduction functions for the Hanford-Livingston (H1-L1) Advanced LIGO network. The tensor overlap reduction function decays rapidly to zero above $f \approx 64\,\text{Hz}$. Standard Advanced LIGO searches for the stochastic background therefore have negligible sensitivity at frequencies above $\sim 64\,\text{Hz}$. The vector and scalar overlap reduction functions, however, remain non-negligible at much higher frequencies. As a result, we will see that Advanced LIGO is generally more sensitive to backgrounds of vector and scalar polarization than to standard tensor backgrounds. For comparison, the right side of Fig. 2 shows the overlap reduction functions for the Hanford-Virgo (H1-V1) baseline. As the separation between Hanford and Virgo is much greater than that between Hanford and Livingston, the Hanford-Virgo overlap reduction functions are generally much smaller in amplitude and more rapidly oscillatory, translating into weaker sensitivity to the stochastic background. Note, however, that the H1-V1 tensor overlap reduction function remains larger in amplitude than H1-L1's at frequencies $f \gtrsim 200\,\text{Hz}$, implying heightened relative sensitivity to tensor backgrounds at high frequencies [56].

We will choose to normalize the cross-correlation statistic $\hat{Y}(f)$ such that

$$\langle \hat{Y}(f) \rangle = \gamma_a(f)\Omega^a(f). \tag{4}$$

Its variance is then [22, 54]

$$\sigma^2(f) = \frac{1}{2T\,df}\left(\frac{10\pi^2}{3H_0^2}\right)^2 f^6 P_1(f)P_2(f). \tag{5}$$

Here, T is the total coincident observation time between detectors, df is the frequency bin-width considered, and $P_i(f)$ is the noise power spectral density of detector i. Note that our normalization, with the overlap reduction functions appearing in the expectation value of $\hat{Y}(f)$, differs from the convention normally adopted in the literature [18, 57, 58]. Our choice, though, will prove far more convenient when studying stochastic backgrounds of mixed gravitational-wave polarizations.

A spectrum of cross-correlation measurements $\hat{Y}(f)$ may be combined to obtain a single broadband signal-to-noise ratio (SNR), given by

$$\text{SNR}^2 = \frac{\left(\hat{Y} \,|\, \gamma_a \Omega^a_M\right)^2}{\left(\gamma_b \Omega^b_M \,|\, \gamma_c \Omega^c_M\right)}, \tag{6}$$

where we have defined the inner product

$$(A \,|\, B) = \left(\frac{3H_0^2}{10\pi^2}\right)^2 2T \int_0^\infty \frac{\tilde{A}^*(f)\tilde{B}(f)}{f^6 P_1(f) P_2(f)} df. \tag{7}$$

In Eq. (6), $\Omega^a_M(f)$ is our adopted model for the energy-density spectrum of the stochastic background. The expected SNR is maximized when this model is equal to the background's true energy-density spectrum. The resulting optimal SNR is given by

$$\text{SNR}^2_{\text{OPT}} = (\gamma_a \Omega^a \,|\, \gamma_b \Omega^b) \tag{8}$$

(see Appendix B for details).

Conventionally, stochastic energy-density spectra are modeled as power laws, such that

$$\Omega^a_M(f) = \Omega^a_0 \left(\frac{f}{f_0}\right)^{\alpha_a}, \tag{9}$$

where Ω^a_0 is the background's amplitude at a reference frequency f_0 and α_a is its spectral index (or slope) [18, 54, 58]. The predicted tensor stochastic background from compact binary coalescences, for instance, is well-modeled by a power law of slope $\alpha_T = 2/3$ in the sensitivity band of Advanced LIGO [57]. For reference, slopes of $\alpha = 0$ and $\alpha = 3$ correspond to scale-invariant energy and strain spectra, respectively. While we will largely assume power-law models in

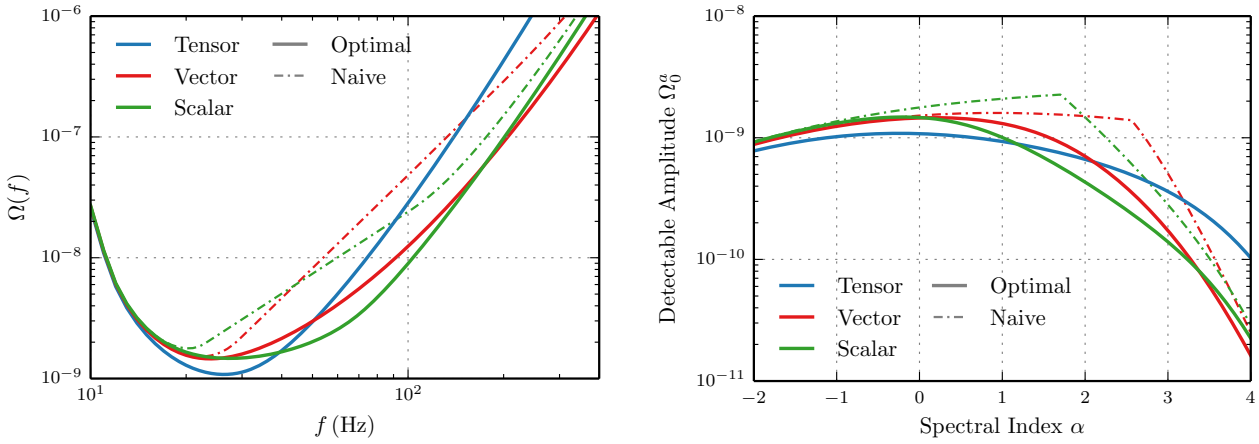

FIG. 3. *Left*: PI curves showing the sensitivity of Advanced LIGO to stochastic backgrounds of tensor, vector, and scalar polarizations (solid blue, red, and green, respectively). Power-law energy-density spectra [Eq. (9)] drawn tangent to the PI curves have expected $\langle \mathrm{SNR}_{\mathrm{OPT}} \rangle = 3$ after three years of observation at design-sensitivity. Also shown are "naive" PI curves for vector and scalar backgrounds (dashed red and green) illustrating the sensitivity of existing search methods optimized only for tensor polarizations. *Right*: Minimum detectable background amplitudes ($\langle \mathrm{SNR}_{\mathrm{OPT}} \rangle = 3$ after three years of observation at design-sensitivity) as a function of spectral index α. For small and negative values of α, Advanced LIGO is approximately equally sensitive to backgrounds of all three polarizations. For large α, Advanced LIGO is instead most sensitive to vector and scalar-polarized backgrounds. The dashed curves show amplitudes detectable with existing "naive" methods. The sensitivity loss between optimal and naive cases is negligible for $\alpha \lesssim 0$, but becomes significant at moderate positive slopes (e.g. $\alpha \sim 2$). The kinks in the naive curves are due to biases incurred when recovering vector and scalar backgrounds with purely-tensor models; see the text for details.

our analysis, in Sect. VI we will explore the potential consequences if this assumption is in fact incorrect (as would be the case, for instance, for a background of unexpectedly massive binary black holes [57]). Throughout this paper we will use the reference frequency $f_0 = 25\,\mathrm{Hz}$.

With the above formalism in hand, we can quantify Advanced LIGO's sensitivity to stochastic backgrounds of alternative polarizations. Plotted on the left side of Fig. 3 are power-law integrated (PI) curves representing Advanced LIGO's optimal sensitivity to power-law backgrounds of pure tensor (solid blue), vector (solid red), and scalar (solid green) modes [59]. The PI curves are defined such that a power-law spectrum drawn tangent to the PI curve will be marginally detectable with $\langle \mathrm{SNR}_{\mathrm{OPT}} \rangle = 3$ after three years of observation with design-sensitivity Advanced LIGO. In general, energy-density spectra lying above and below the PI curves are expected to have optimal SNRs greater and less than 3, respectively. In the right side of Fig. 3, meanwhile, the solid curves trace the power-law amplitudes required for marginal detection ($\langle \mathrm{SNR}_{\mathrm{OPT}} \rangle = 3$ after three years of observation) as a function of spectral index.

For spectral indices $\alpha \lesssim 0$, Advanced LIGO is approximately equally sensitive to backgrounds of all three polarizations. When $\alpha = 0$, for instance, the minimum optimally-detectable tensor amplitude is $\Omega_0^T = 1.1 \times 10^{-9}$, while the minimum detectable vector and scalar amplitudes are $\Omega_0^{V/S} = 1.5 \times 10^{-9}$. This comparable sensitivity is due to the fact that the tensor, vector, and scalar overlap reduction functions are all of approximately equal magnitude at low frequencies (see Fig. 2). At high frequencies, on the other hand, Advanced LIGO's tensor overlap reduction function decays more rapidly than the vector and scalar overlap reduction functions. As a result, Advanced LIGO is more sensitive to vector and scalar backgrounds of large, positive slope than to tensor backgrounds of similar spectral shape. In Fig. 3.a, for instance, the vector and scalar PI curves are seen to lie an order of magnitude below the tensor PI curve at frequencies above $f \sim 300\,\mathrm{Hz}$. The constraints that Advanced LIGO can place on positively-sloped vector and scalar backgrounds are therefore as much as an order of magnitude more stringent than those that can be placed on tensor backgrounds of similar slope.

We emphasize that the Advanced LIGO network's relative sensitivities to tensor, vector, and scalar-polarized backgrounds are due purely to its geometry, rather than properties of the backgrounds themselves. If we were instead to consider the Hanford-Virgo baseline, for instance, the right-hand side of Fig. 2 shows that at high frequencies the H1-V1 pair is least sensitive to scalar polarizations, whereas the H1-L1 baseline is least sensitive to tensor modes.

So far we have discussed only Advanced LIGO's *optimal* sensitivity to stochastic backgrounds of alternative polarizations. Existing stochastic searches, though, are *not* optimized for such backgrounds, instead using models $\Omega_M^\alpha(f)$ that allow only for tensor gravitational-wave polarizations. The dashed curves in Fig. 3 illustrate Advanced LIGO's "naive" sensitivity to backgrounds of alternative polarizations when incorrectly assuming a purely-tensor model. The loss in sensitivity between the optimal and "naive" searches varies greatly with different spectral indices. Sensitivity loss is relatively minimal

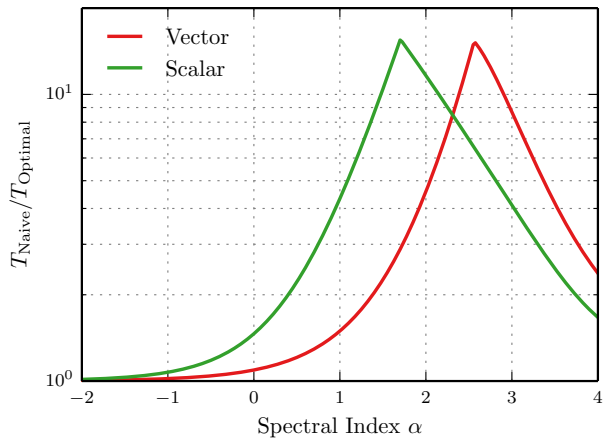

FIG. 4. The fractional increase in observing time required for Advanced LIGO to make a detection of vector (red) and scalar (green) backgrounds using existing search techniques, as a function of their spectral index α. The sharp kinks in each curve are due to biases incurred when fitting vector and scalar backgrounds with a purely-tensor model; see the text for details.

for slopes $\alpha \lesssim 0$. When $\alpha = 0$, for example, the minimum detectable scalar amplitude rises from $\Omega_0^S = 1.5 \times 10^{-9}$ in the optimal case to 1.8×10^{-9} in the naive case, an increase of 20%. Thus, a flat scalar background that is optimally detectable by Advanced LIGO may still be detected using existing techniques tailored to tensor polarizations. The SNR penalty is more severe for stochastic backgrounds of moderate positive slope. For $\alpha = 2$, Advanced LIGO can optimally detect a scalar background of amplitude $\Omega_0^S = 4.3 \times 10^{-10}$, while existing methods would detect only a background of amplitude $\Omega_0^S = 1.5 \times 10^{-9}$, a factor of 3.5 larger.

Since the SNR of the stochastic search accumulates only as SNR $\propto \sqrt{T}$, even a small decrease in sensitivity can result in a somewhat severe increase in the time required to make a detection. To illustrate this, Fig. 4 shows the ratio $T_{\rm Naive}/T_{\rm Optimal}$ between the observing times required for Advanced LIGO to detect vector (red) and scalar (green) backgrounds using existing "naive" methods and optimal methods. Although we noted above that existing methods incur little sensitivity loss to flat scalar backgrounds, the detection of such backgrounds would nevertheless require at least 50% more observing time with existing searches. Naive detection of a scalar background with $\alpha = 2$, for comparison, would require nearly twelve times the observing time.

Even in the case of minimal SNR loss, the use of existing detection methods poses another risk: if a vector or scalar background is detected, we may remain entirely unaware that the background does indeed violate general relativity (see Sect. IV below). Furthermore, we would suffer from severe "stealth bias," unknowingly recovering heavily-biased estimates of the amplitude and spectral index of the stochastic background [60, 61]. Vector and scalar backgrounds with large, positive slopes are best fit by tensor models with even larger slopes. Meanwhile, best-fit tensor spectral indices are biased towards much smaller values when recovering non-GR backgrounds with small or negative slopes. The sharp kinks seen in Figs. 3 and 4 (at $\alpha_S \approx 1.75$ and $\alpha_V \approx 2.5$) mark the transition between these two regimes.

IV. IDENTIFYING ALTERNATIVE POLARIZATIONS

We have seen in Sect. III that, even when using existing methods assuming only standard tensor polarizations, Advanced LIGO may still be capable of detecting a stochastic background of vector or scalar modes (albeit after potentially much longer observation times). Detection is only the first of two hurdles, though. Once the stochastic background has been detected, we will still need to establish whether it is entirely tensor-polarized, or if it contains vector or scalar-polarized gravitational waves.

Since tensor, vector, and scalar gravitational-wave polarizations each enter into cross-correlation measurements [Eq. (3)] with unique overlap reduction functions, the polarization content of a detected stochastic background is in principle discernible from the spectral shape of $\hat{Y}(f)$. As an example, Fig. 5 shows simulated cross-correlation measurements $\hat{Y}(f)$ for both purely tensor (blue) and purely scalar-polarized (green) backgrounds after three years of observation with design-sensitivity Advanced LIGO. The left-hand side shows measurements of particularly loud backgrounds, with spectra $\Omega^T(f) = \Omega^S(f) = 10^{-7}(f/f_0)^{2/3}$. The dashed curves trace the expectation values $\langle \hat{Y}(f) \rangle$ of the cross-correlation spectra for each case, while the solid curves show actual measured values. The alternating signs (positive or negative) of each spectrum are determined by the tensor and scalar overlap reduction functions, which have zero-crossings at different characteristic frequencies (see Fig. 2). As a result, tensor and scalar-polarized signals each impart a unique shape to the cross-correlation spectra, offering a means of discriminating between the two cases.

The backgrounds considered in the left side of Fig 5, though, are unphysically loud, with $\text{SNR}_{\text{OPT}} = 174$ and 143 for the tensor and scalar backgrounds, respectively, at design-sensitivity. A tensor background of this amplitude would have been detectable with the standard isotropic search over Advanced LIGO's O1 observing run [18]. Since stochastic searches accumulate SNR over time, the first detection of the stochastic background will necessarily be marginal; in this case the presence of alternative gravitational-wave polarizations would not be clear. To demonstrate this, the right side of Fig. 5 shows the simulated recovery of weaker tensor and scalar backgrounds of spectral shape $\Omega(f) = 4 \times 10^{-9}(f/f_0)^{2/3}$, again after three years of observation with Advanced LIGO. Advanced LIGO would still make a strong detection of each background, with $\text{SNR}_{\text{OPT}} = 6.9$ and 6.5 for the tensor and scalar backgrounds. The backgrounds' polarization content, however, is no longer obvious. Note that, even using naive search methods, design-sensitivity Advanced LIGO would still make a detection of the scalar example with SNR $= 3.9$.

When assuming *a priori* that the stochastic background is

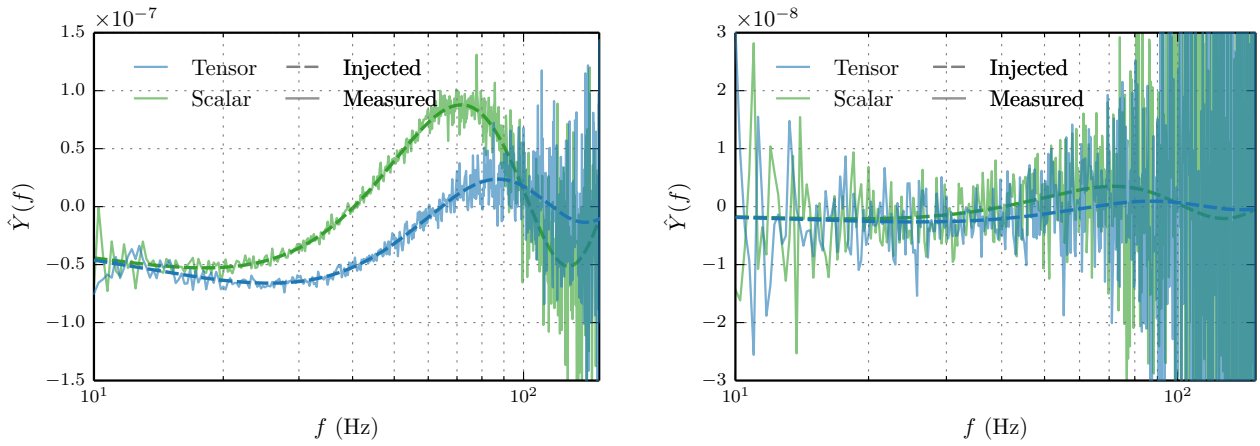

FIG. 5. *Left*: Simulated cross-correlation measurements $\hat{Y}(f)$ for purely tensor (blue) and purely scalar (green) stochastic backgrounds, recovered after three years of observation with design-sensitivity Advanced LIGO. Although the underlying backgrounds have identical spectral shapes $\Omega(f) = 10^{-7}(f/f_0\,\mathrm{Hz})^{2/3}$, the measured spectra each show distinct modulations characteristic of the tensor and scalar overlap reduction functions. *Right*: Simulated recovery of purely tensor and scalar backgrounds with weaker amplitudes $\Omega(f) = 4 \times 10^{-9}(f/f_0\,\mathrm{Hz})^{2/3}$. While each background would be confidently detected by existing search techniques, the characteristic amplitude modulations and hence the polarization content of each simulated background are no longer evident.

purely tensor-polarized, any vector or scalar components detected with existing techniques would be mistaken for ordinary tensor modes. Not only would vector or scalar components fail to be identified, but, as discussed in Sect. III, they would heavily bias parameter estimation of the tensor energy-density spectrum. If we wish to test general relativity with the stochastic background, we will therefore need to develop new tools in order to formally quantify the presence (or absence) of vector or scalar polarizations. Additionally, while we have so far investigated only backgrounds of pure tensor, vector, or scalar polarization, most plausible alternative theories of gravity will predict backgrounds of *mixed* polarization, with vector or scalar components in addition to a tensor component. Any realistic approach must therefore be able to handle a stochastic background of completely generic polarization content.

Our approach will be to detect and classify the stochastic background using Bayesian model selection. First, we will define an odds ratio $\mathcal{O}^{\mathrm{SIG}}_{\mathrm{N}}$ between signal (SIG) and noise (N) hypotheses to determine if a stochastic background (of any polarization) has been observed. Once a background is detected, we then construct a second odds ratio $\mathcal{O}^{\mathrm{NGR}}_{\mathrm{GR}}$ to determine if the background contains only tensor polarization (GR hypothesis) or if there is evidence of alternative polarizations (the NGR hypothesis). We describe the definition and construction of $\mathcal{O}^{\mathrm{SIG}}_{\mathrm{N}}$ and $\mathcal{O}^{\mathrm{NGR}}_{\mathrm{GR}}$ in Appendix C. Unlike existing detection methods that assume a pure tensor background, our scheme allows for the detection of generically-polarized stochastic backgrounds. It encapsulates the optimal detection of tensor, vector, and scalar polarizations as described in Sect. III, and moreover enables the detection of more complex backgrounds of mixed polarization.

To compute the odds ratios $\mathcal{O}^{\mathrm{SIG}}_{\mathrm{N}}$ and $\mathcal{O}^{\mathrm{NGR}}_{\mathrm{GR}}$, we use the `PyMultiNest` package [62], which implements a Python wrapper for the nested sampling software `MultiNest` [63–65]. `MultiNest`, an implementation of the nested sampling algorithm [66, 67], is designed to efficiently evaluate Bayesian evidences [see Eq. (C1)] in high-dimensional parameter spaces, even in the case of large and possibly-curving parameter degeneracies. At little additional computational cost, `MultiNest` also returns posterior probabilities for each model parameter, allowing for parameter estimation in addition to model selection. Details associated with running `MultiNest` are given in Appendix D.

A. Backgrounds of Single Polarizations

As a first demonstration of this machinery, we explore the simple cases of purely tensor, vector, or scalar-polarized stochastic backgrounds. Shown in Fig. 6 are distributions of odds ratios $\mathcal{O}^{\mathrm{SIG}}_{\mathrm{N}}$ and $\mathcal{O}^{\mathrm{NGR}}_{\mathrm{GR}}$ obtained for simulated observations of both tensor and scalar backgrounds, each of slope $\alpha = 2/3$ (the characteristic slope of a tensor binary black hole background). For each polarization, we consider two choices of amplitude, corresponding to $\langle \mathrm{SNR}_{\mathrm{OPT}} \rangle = 5$ and 10 after three years of observation with design-sensitivity Advanced LIGO. For comparison, the hatched grey distributions show odds ratios obtained in the presence of pure Gaussian noise.

As seen in the left-hand side of Fig. 6, Gaussian noise yields a narrow odds ratio distribution centered at $\ln \mathcal{O}^{\mathrm{SIG}}_{\mathrm{N}} = -1.1$. In contrast, the simulated observations of tensor and scalar backgrounds yield large, positive odds ratios, well-separated from Gaussian noise. Note that the tensor and scalar distributions lie nearly on top of one another, as $\mathcal{O}^{\mathrm{SIG}}_{\mathrm{N}}$ depends primarily on the optimal SNR of a background and not its polarization content.

The right-hand side of Fig. 6, in turn, shows the odds ra-

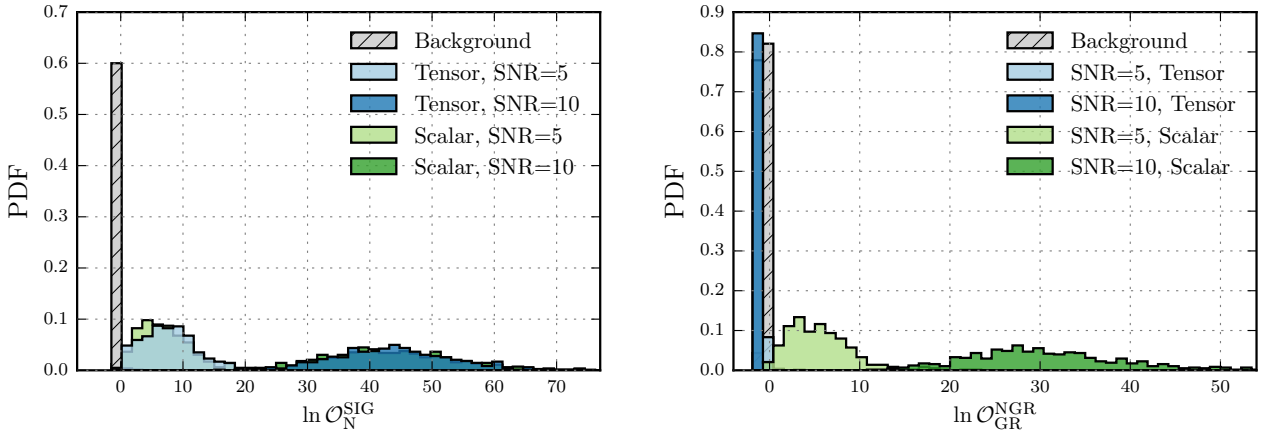

FIG. 6. *Left*: Distributions of odd ratios $\mathcal{O}_{\rm N}^{\rm SIG}$ between signal and noise hypotheses for simulated observations of tensor (blue) and scalar (green) stochastic backgrounds of slope $\alpha = 2/3$, assuming three years of observation with design-sensitivity Advanced LIGO. We consider two different strengths for each polarization, corresponding to $\langle {\rm SNR}_{\rm OPT} \rangle = 5$ and 10. For each background strength, the tensor and scalar odds ratios lie nearly on top of one another. Also shown is the background distribution of odds ratios obtained when observing pure Gaussian noise (hatched grey). In the presence of a stochastic background, the recovered odds ratios grow as $\ln \mathcal{O}_{\rm N}^{\rm SIG} \propto {\rm SNR}_{\rm OPT}^2$, showing increasingly large preference for the signal hypothesis. *Right*: Odds ratios $\mathcal{O}_{\rm GR}^{\rm NGR}$ between NGR and GR hypotheses obtained for the same set of simulated Advanced LIGO observations. In the presence of a tensor-polarized background, we recover narrow distributions of odds ratios centered at $\ln \mathcal{O}_{\rm GR}^{\rm NGR} \approx -1.5$, reflecting consistency with the GR hypothesis. A scalar background, on the other hand, yields large positive odds ratios, correctly showing a strong preference for our NGR hypothesis.

tios $\mathcal{O}_{\rm GR}^{\rm NGR}$ quantifying the evidence for alternative polarization modes. In the case of pure Gaussian noise, we again see a narrow distribution of odds ratios, centered at $\ln \mathcal{O}_{\rm GR}^{\rm NGR} = -0.50$. In the absence of informative data, our analysis thus slightly favors the GR hypothesis. This can be understood as a consequence of the implicit Bayesian "Occam's factor," which penalizes the more complex NGR hypothesis over the simpler GR hypothesis. Simulated observations of scalar backgrounds, in turn, yield large positive values for $\ln \mathcal{O}_{\rm GR}^{\rm NGR}$, correctly preferencing the NGR hypothesis. In contrast, pure tensor backgrounds yield negative $\ln \mathcal{O}_{\rm GR}^{\rm NGR}$. Interestingly, the recovered odds ratios do not grow increasingly negative with larger tensor amplitudes, but instead saturate at $\ln \mathcal{O}_{\rm GR}^{\rm NGR} \approx -1.5$. This reflects the fact that a non-detection of vector or scalar polarizations can never strictly rule out their presence, but only place an upper limit on their amplitudes. In other words, a strong detection of a pure tensor stochastic background cannot provide evidence *for* the GR hypothesis, but at best only offers no evidence *against* it. This behavior is in part due to our choice of amplitude priors, which allow for finite but immeasurably small vector and scalar energy densities (see Appendix C).

Figure 7 illustrates more generally how $\mathcal{O}_{\rm N}^{\rm SIG}$ (left column) and $\mathcal{O}_{\rm GR}^{\rm NGR}$ (right column) scale with the amplitudes of purely tensor (blue), vector (red), and scalar (green) stochastic backgrounds. Black points mark odds ratios computed from individual realizations of simulated data, while the solid curves and shaded regions trace their smoothed mean and standard deviation. We again see $\ln \mathcal{O}_{\rm N}^{\rm SIG}$ increasing monotonically with injected amplitude for all three polarizations. Specifically, $\mathcal{O}_{\rm N}^{\rm SIG}$ depends inversely on the noise-hypothesis likelihood [defined by Eq. (C5)] and therefore scales as

$$\ln \mathcal{O}_{\rm N}^{\rm SIG} \propto {\rm SNR}_{\rm OPT}^2. \tag{10}$$

As seen earlier in Fig. 6, $\ln \mathcal{O}_{\rm GR}^{\rm NGR}$ saturates at -1.5 for loud tensor backgrounds. In the case of vector and scalar backgrounds, on the other hand, $\ln \mathcal{O}_{\rm GR}^{\rm NGR}$ grows quadratically with increasing amplitude. In particular, $\ln \mathcal{O}_{\rm GR}^{\rm NGR}$ is proportional to the squared SNR of the *residuals* between the observed $\hat{Y}(f)$ and the best-fit tensor model. We begin to see a strong preference for the NGR hypothesis when these residuals become statistically significant.

B. Backgrounds of Mixed Polarization

So far we have considered only cases of pure tensor, vector, or scalar polarization. Plausible alternative theories of gravity, however, would typically predict a mixed background of multiple polarization modes. How does our Bayesian machinery handle a background of mixed polarization? To answer this question, we will investigate backgrounds of mixed tensor and scalar polarization. Figure 8 shows values of $\mathcal{O}_{\rm N}^{\rm SIG}$ and $\mathcal{O}_{\rm GR}^{\rm NGR}$ (left and right-hand sides, respectively) as a function of the amplitude of each polarization. While we allow the amplitudes to vary, we fix the tensor and scalar slopes to $\alpha_T = 2/3$ and $\alpha_S = 0$, as predicted for binary black hole backgrounds under scalar-tensor theories (see Appendix E).

In the left side Fig. 8, the recovered values of $\ln \mathcal{O}_{\rm N}^{\rm SIG}$ simply trace contours of total energy. Thus the *detectability* of a mixed background depends only on its total measured energy, rather than its polarization content. Meanwhile, three

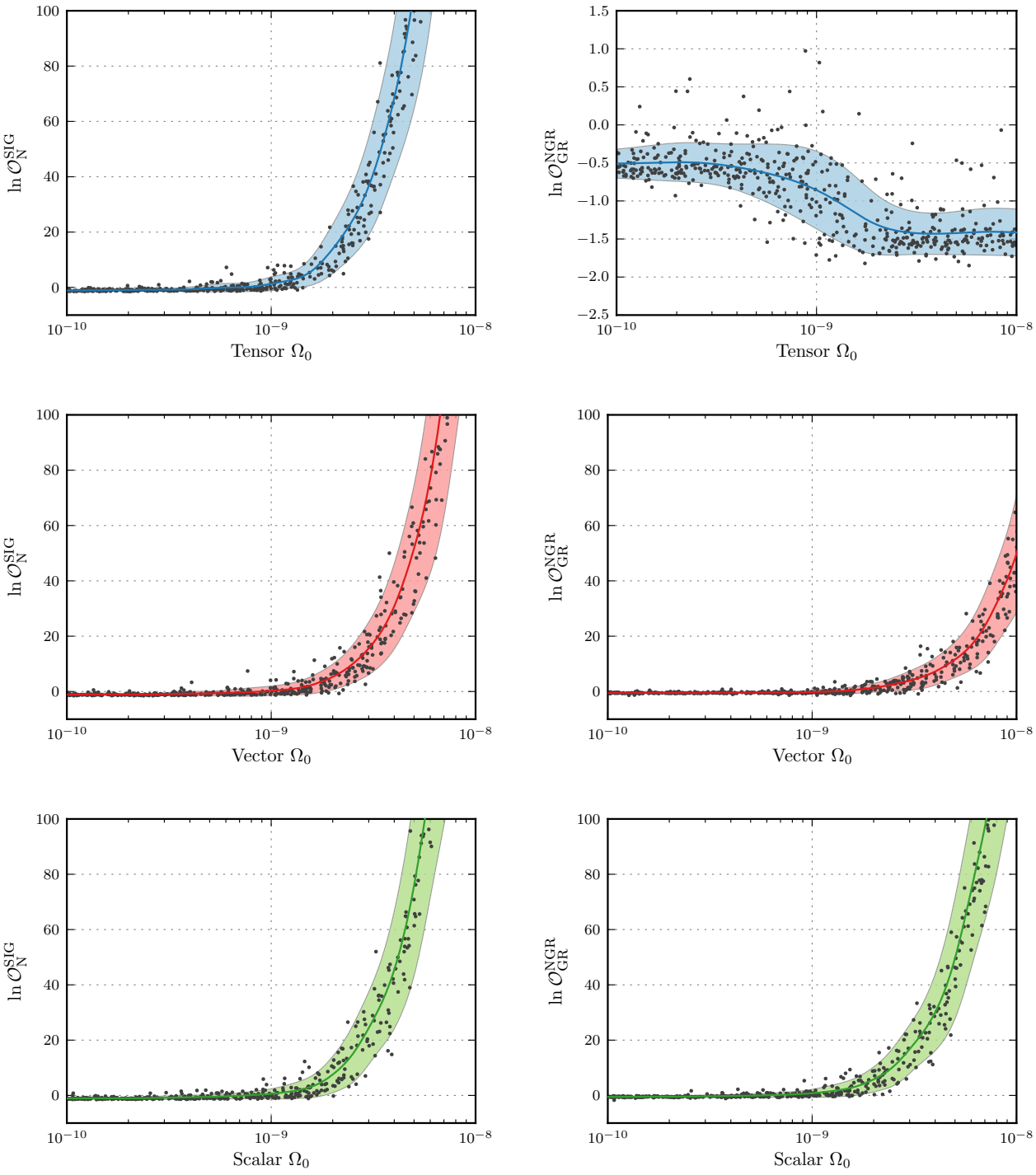

FIG. 7. Odds ratios $\mathcal{O}_{\rm N}^{\rm SIG}$ (left) and $\mathcal{O}_{\rm GR}^{\rm NGR}$ (right) for simulated Advanced LIGO observations of purely tensor (blue), vector (red), and scalar (green) polarized stochastic backgrounds. Within each plot, we show 1000 simulated observations, with random log-amplitudes chosen uniformly over the range $-10 < \log \Omega_0 < -7$. Black points mark the results from individual realizations, while the solid curves and shaded regions show the moving mean and standard deviations (smoothed with a Gaussian kernel) of these realizations. For each polarization, $\log \mathcal{O}_{\rm N}^{\rm SIG}$ scales quadratically with the amplitude of the stochastic background. Similarly, $\log \mathcal{O}_{\rm GR}^{\rm NGR}$ scales quadratically with vector and scalar amplitude. For tensor backgrounds, however, $\log \mathcal{O}_{\rm GR}^{\rm NGR}$ instead saturates at approximately -1.5.

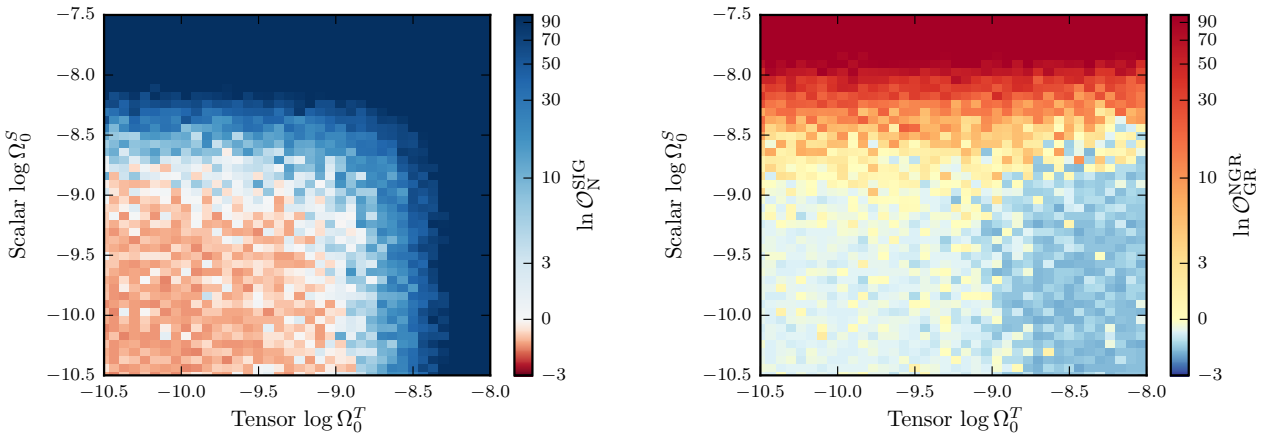

FIG. 8. Odds ratios for simulated Advanced LIGO measurements of stochastic backgrounds containing both tensor and scalar polarizations, assuming three years of observation at design sensitivity. The tensor and scalar components have slopes $\alpha_T = 2/3$ and $\alpha_S = 0$, respectively, following predictions for the background due to black hole binaries (see Appendix E). *Left*: Odds ratios between signal and noise hypotheses. The observed values of $\mathcal{O}_{\rm N}^{\rm SIG}$ trace contours in total background energy. Thus the detectability of a background depends largely on its total power, not its polarization content. *Right*: Odds ratios $\mathcal{O}_{\rm GR}^{\rm NGR}$ between NGR and GR hypotheses. Advanced LIGO would successfully identify the presence of the scalar background component when $\Omega_0^S \gtrsim 10^{-8.5}$. LIGO's sensitivity to the scalar component is nearly independent of the strength of the tensor component; the minimum identifiable scalar amplitude Ω_0^S rises only slightly with increasing Ω_0^T.

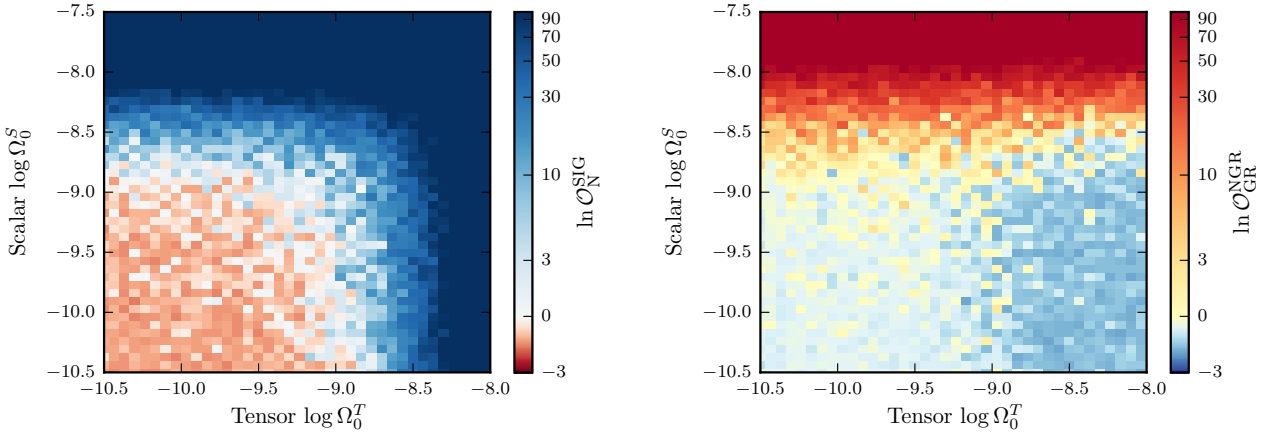

FIG. 9. As above, but for simulated three-year observations with the joint Advanced LIGO-Virgo network at design sensitivity. Despite the inclusion of Advanced Virgo, the sensitivity of this three-detector network is nearly identical to that of Advanced LIGO alone.

distinct regions are observed in the right-hand subplot. First, for small tensor and scalar amplitudes ($\log \Omega_0^T \lesssim -9.5$ and $\log \Omega_0^S \lesssim -9$), we obtain $\ln \mathcal{O}^{\rm NGR}_{\rm GR} \sim -0.5$. In this region, the mixed background simply cannot be detected and so we recover the slight Occam's bias towards the GR hypothesis as noted above. Secondly, for small scalar and large tensor amplitudes ($\log \Omega_0^T \gtrsim -9$), the recovered odds ratios decrease to $\ln \mathcal{O}^{\rm NGR}_{\rm GR} \sim -1$. This corresponds to the detection of the tensor component alone; the decrease in odds ratios is the same behavior previously seen in Figs. 6 and 7. Finally, when Ω_0^S is large, the scalar component is detectable and the recovered $\ln \mathcal{O}^{\rm NGR}_{\rm GR}$ increases rapidly to large, positive values. The threshold value of Ω_0^S at which $\ln \mathcal{O}^{\rm NGR}_{\rm GR}$ becomes positive shows only little dependence on the amplitude of any tensor background which might also be present. When Ω_0^T is small, for instance, scalar amplitudes of size $\log \Omega_0^S \gtrsim -8.6$ are required to preference the NGR model. When Ω_0^T is large, this requirement increases only slightly to $\log \Omega_0^S \gtrsim -8.4$. Thus, we should expect Advanced LIGO to be able to both detect and *identify as non-tensorial* a flat scalar background of amplitude $\log \Omega_0^S \gtrsim -8$, regardless of the presence of an additional tensor component.

It should be pointed out that positive $\log \mathcal{O}^{\rm NGR}_{\rm GR}$ indicates only that there exists evidence for alternative polarizations. From the odds ratio alone we cannot infer which specific polarizations – vector and/or scalar – are present in the background. While we found above that Advanced LIGO can identify mixed tensor-scalar backgrounds as non-tensorial when $\log \Omega_0^S \gtrsim -8$, this *does not* imply that we can successfully identify the scalar component as such, only that our measurements are not consistent with tensor polarization alone (see Sect. V).

The future addition of new gravitational wave detectors, beginning with Advanced Virgo in 2017, will extend the reach of stochastic searches and help to break degeneracies between backgrounds of different polarizations. It is therefore interesting to investigate to what degree the introduction of Advanced Virgo will improve the above results. Given detectors indexed by $i \in \{1, 2, ...\}$, the total SNR of a stochastic background is the quadrature sum of SNRs from each detector pair:

$$\mathrm{SNR}^2 = \sum_i \sum_{j>i} \mathrm{SNR}^2_{ij}, \tag{11}$$

where each SNR_{ij} is computed following Eq. (6). Naively, the SNR with which a background is observed is expected to increase as $\mathrm{SNR} \propto \sqrt{N}$, where N is the total number of available detector pairs (three in the case of the Advanced LIGO-Virgo network). However, both the Hanford-Virgo and Livingston-Virgo pairs exhibit reduced sensitivity to the stochastic background due to their large physical separations. This fact is reflected in their respective overlap reduction functions, which are smaller in magnitude than the Hanford-Livingston overlap reduction functions by a factor of several (see Fig. 2).

Given three independent detector pairs (and hence three independent measurements at each frequency), one can in principle directly solve for the unknown tensor, vector, and scalar contributions to the background in each frequency bin [12, 22–24]. This component separation scheme can be performed without resorting to a model for the stochastic energy-density spectrum. However, frequency-by-frequency component separation is unlikely to be successful using the LIGO-Virgo network, due to the large uncertainties in the measured background at each frequency. Instead, when considering joint Advanced LIGO-Virgo observations we will again apply the Bayesian framework introduced above, leveraging measurements made at many frequencies in order to constrain the power-law amplitude and slope of each polarization mode.

To quantify the extent to which Advanced Virgo aids in the detection of the stochastic background, we again consider simulated observations of a mixed tensor (slope $\alpha_T = 2/3$) and scalar (slope $\alpha_S = 0$) background, this time with a three-detector Advanced LIGO-Virgo network. Our Bayesian formalism is easily extended to accommodate the case of multiple detector pairs; details are given in Appendix C. The odds ratios obtained from our simulated Advanced LIGO-Virgo observations are shown in Fig. 9 for various tensor and scalar amplitudes. The inclusion of Advanced Virgo yields no clear improvement over the Advanced LIGO results in Fig. 8. Due to its large distance from LIGO, Advanced Virgo does not contribute more than a small fraction of the total observed SNR. As a result, the combined Hanford-Livingston-Virgo network both detects (as indicated with $\mathcal{O}^{\rm SIG}_{\rm N}$) and identifies (via $\mathcal{O}^{\rm NGR}_{\rm GR}$) the scalar background component with virtually the same sensitivity as the Hanford-Livingston network alone.

V. PARAMETER ESTIMATION ON MIXED BACKGROUNDS

Parameter estimation will be the final step in a search for a stochastic background of generic polarization. If a gravitational-wave background is detected (as inferred from $\mathcal{O}^{\rm SIG}_{\rm N}$), how well can Advanced LIGO constrain the properties of the background? Alternatively, if no detection is made, what upper limits can Advanced LIGO place on the background amplitudes of each polarization mode? We investigate these questions through three case studies: an observation of pure Gaussian noise, a standard tensor stochastic background, and a background of mixed tensor and scalar polarizations. The simulated background parameters used for each case are listed in Table I.

When performing model selection above, the odds ratios $\mathcal{O}^{\rm SIG}_{\rm N}$ and $\mathcal{O}^{\rm NGR}_{\rm GR}$ were constructed by independently allowing for each combination of tensor, vector, and scalar modes (see Appendix C). Parameter estimation, meanwhile, must be performed in the context of a specific background model. For the case studies below, we will adopt the broadest possible hypothesis, allowing for all three polarization modes (the TVS hypothesis in Appendix C). This choice will allow us to place simultaneous constraints on the presence of tensor, vector, and scalar polarizations in the stochastic background. Parameter estimation is achieved using `MultiNest`, which returns samples drawn from the measured posterior distributions.

There are several key subtleties that must be understood when interpreting the parameter estimation results presented

TABLE I. Stochastic background parameters used for each case study presented. For each case, the vector amplitude is set to zero. Also shown are the odds ratios computed for each simulated observation.

Case	$\log\Omega_0^T$	α_T	$\log\Omega_0^S$	α_S	H1-L1		H1-L1-V1	
					$\ln\mathcal{O}_{\rm N}^{\rm SIG}$	$\ln\mathcal{O}_{\rm GR}^{\rm NGR}$	$\ln\mathcal{O}_{\rm N}^{\rm SIG}$	$\ln\mathcal{O}_{\rm GR}^{\rm NGR}$
1	—	—	—	—	-1.4	-0.5	-1.4	-0.6
2	-8.78	0.67	—	—	6.0	-1.2	7.2	-1.4
3	-8.78	0.67	-8.61	0.0	38.8	4.3	39.4	4.6

below. First, whereas standard tensor upper limits are conventionally defined with respect to a single, fixed slope [18, 58], we will quote amplitude limits obtained *after* marginalization over spectral index. This approach concisely combines information from the entire posterior parameter space to offer a single limit on each polarization considered. As a result, however, our simulated upper limits presented here should not be directly compared to those from standard searches for tensor backgrounds. Secondly, parameter estimation results are contingent upon the choice of a specific model. While we will demonstrate parameter estimation results under our TVS hypothesis (see Appendix C), other hypotheses may be better suited to answering other experimental questions. For example, if we were specifically interested in constraining scalar-tensor theories (which *a priori* do not allow vector polarizations), we would instead perform parameter estimation under the TS hypothesis. And if our goal was to perform a standard stochastic search for a purely tensor-polarized background, we would restrict to the T hypothesis. Although these various hypotheses all contain an analogous parameter Ω_0^T, the resulting upper limits on Ω_0^T will generically be different in each case. In short, different experimental questions will yield different answers.

Case 1: Gaussian Noise

First, we consider the case of pure noise, producing a simulated three-year observation of Gaussian noise at Advanced LIGO's design sensitivity. The resulting TVS posteriors are shown in Fig. 10. The colored histograms along the diagonal show the marginalized 1D posteriors for the amplitudes and slopes of the tensor, vector, and scalar components (blue, green, and red, respectively). The priors placed on each parameter are indicated with a dashed grey curve. Above each posterior we quote the median posterior value as well as $\pm 34\%$ credible limits. The remaining subplots illustrate the joint 2D posteriors between each pair of parameters.

For this simulated Advanced LIGO observation, we obtain $\log\mathcal{O}_{\rm N}^{\rm SIG} = -1.4$, consistent with a null detection. Accordingly, the posteriors on Ω_0^T, Ω_0^V, and Ω_0^S each coincide with the lower bound of our amplitude prior (at $\log\Omega_{\rm Min} = -13$). Meanwhile, the posteriors on spectral indices α_T, α_V, and α_S simply recover our chosen prior. The 95% credible upper limits on each amplitude are $\log\Omega_0^T < -10.1$, $\log\Omega_0^V < -9.9$, and $\log\Omega_0^S < -10.0$.

In Fig. 11 we show the posteriors obtained if we additionally include design-sensitivity Advanced Virgo (incorporating simulated measurements for the HV and LV detector pairs). For reference, the grey histograms show the posteriors from Fig. 10 obtained by Advanced LIGO alone. The Advanced LIGO-Virgo posteriors are nearly identical to those obtained from Advanced LIGO alone, with 95% credible upper limits of $\log\Omega_0^T < -10.1$, $\log\Omega_0^V < -10.0$, and $\log\Omega_0^S < -10.2$. In the case of a null-detection, then, the inclusion of Advanced Virgo does not notably improve the upper limits placed on the amplitudes of tensor, vector, and scalar backgrounds.

Case 2: Tensor Background

Next, we produce a simulated observation of a pure tensor background with amplitude $\log\Omega_0^T = -8.78$ and spectral index $\alpha_T = 2/3$. The amplitude is chosen such that the background would be detected by Advanced LIGO with expected $\langle{\rm SNR}_{\rm OPT}\rangle = 5$ after three years of observation at design-sensitivity. The odds ratios obtained for this simulated observation are $\log\mathcal{O}_{\rm N}^{\rm SIG} = 6.0$ and $\log\mathcal{O}_{\rm GR}^{\rm NGR} = -1.2$, indicating a moderately strong detection consistent with general relativity.

The corresponding parameter posteriors are shown in Fig. 12. In this case, the injected parameter values are shown via dot-dashed black lines. The $\log\Omega_0^T$ posterior is strongly peaked near the true value, with a central 68% credible interval of $-9.1 \leq \log\Omega_0^T \leq -8.8$ and a median value of $\log\Omega_0^T = -8.9$. The vector and scalar amplitudes, in turn, are consistent with the lower bound on our prior, with 95% credible upper limits of $\log\Omega_0^V < -8.9$ and $\log\Omega_0^S < -9.4$. In the joint posteriors, though, we see evidence of degeneracy between the three amplitudes, most noticeably between the tensor and vector modes. When observing with Advanced LIGO alone, these degeneracies persist even at high SNRs, as will be illustrated in the remaining case below.

The parameter estimation results when additionally including Advanced Virgo are given in Fig. 13. Once again, the grey histograms show parameter estimation results from Advanced LIGO alone. Although Virgo does not improve our confidence in the detection, it *can* serve to break degeneracies present between different polarization modes. We begin to see this behavior in Fig. 13, in which the vector and scalar log-amplitude posteriors are pushed to smaller values in the joint LIGO-Virgo analysis. When including Advanced Virgo, we obtain a marginally tighter 68% credible interval of $-9.0 \leq \log\Omega_0^T \leq -8.8$ on the tensor amplitude, and improved upper limits of $\log\Omega_0^V < -9.2$ and $\log\Omega_0^S < -9.6$ on vector and scalar amplitudes.

Case 3: Tensor and Scalar ($\alpha_S = 0$) Backgrounds

As discussed above, most alternative theories of gravity would predict a stochastic background of mixed polarization. For our final case study, we therefore consider a mixed background with both tensor ($\log\Omega_0^T = -8.78$ and $\alpha_T = 2/3$)

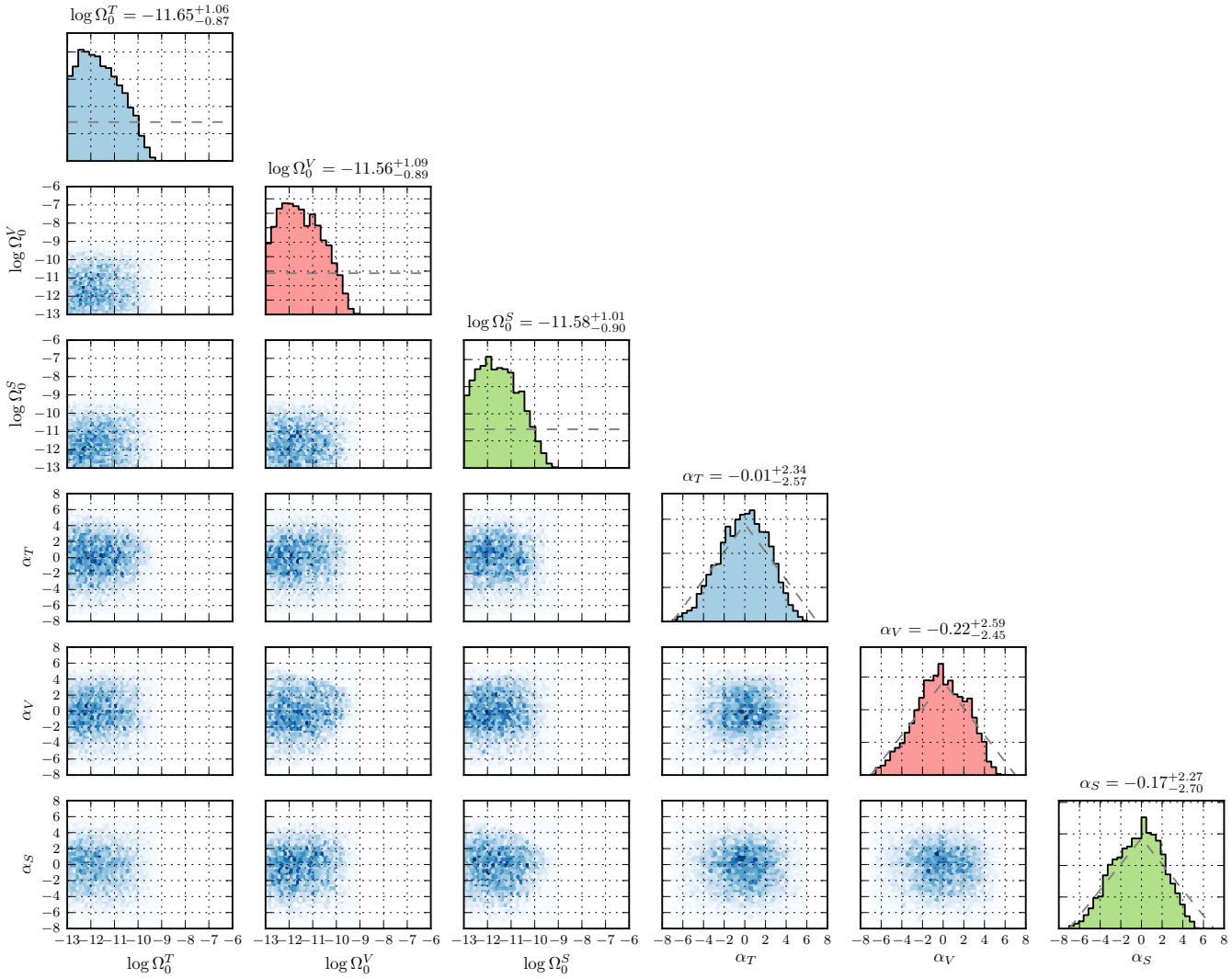

FIG. 10. Posteriors obtained for a simulated Advanced LIGO observation of pure Gaussian noise (Case 1 in Table I), under the TVS hypothesis. The subplots along the diagonal show marginalized posteriors for the amplitudes and slopes of the tensor, vector, and scalar backgrounds (blue, red, and green, respectively), while the remaining subplots show the 2D posterior between each pair of parameters. Each amplitude posterior is consistent with our lower prior bound, reflecting the non-detection of a stochastic background.

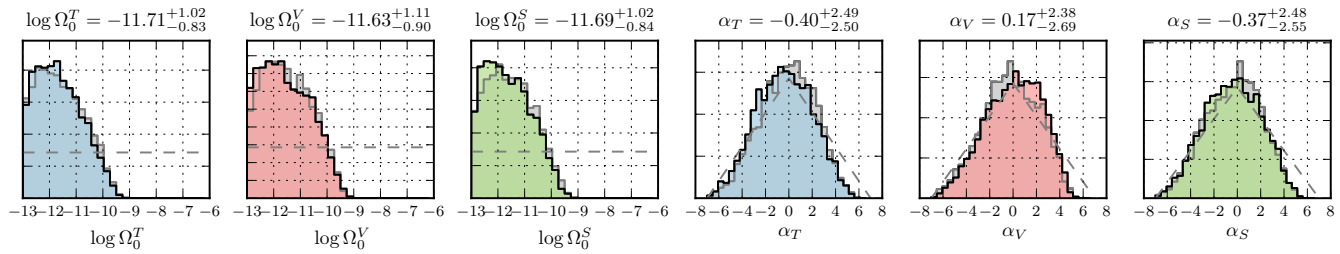

FIG. 11. Marginalized amplitude and slope posteriors for the Gaussian noise observation in Fig. 10, after the additional inclusion of design-sensitivity Advanced Virgo. For reference, the light grey histograms show the Advanced LIGO-only results from Fig. 10. As above, dashed grey lines show the priors placed on each parameter. We see that the inclusion of Advanced Virgo does not significantly affect the parameter estimation results.

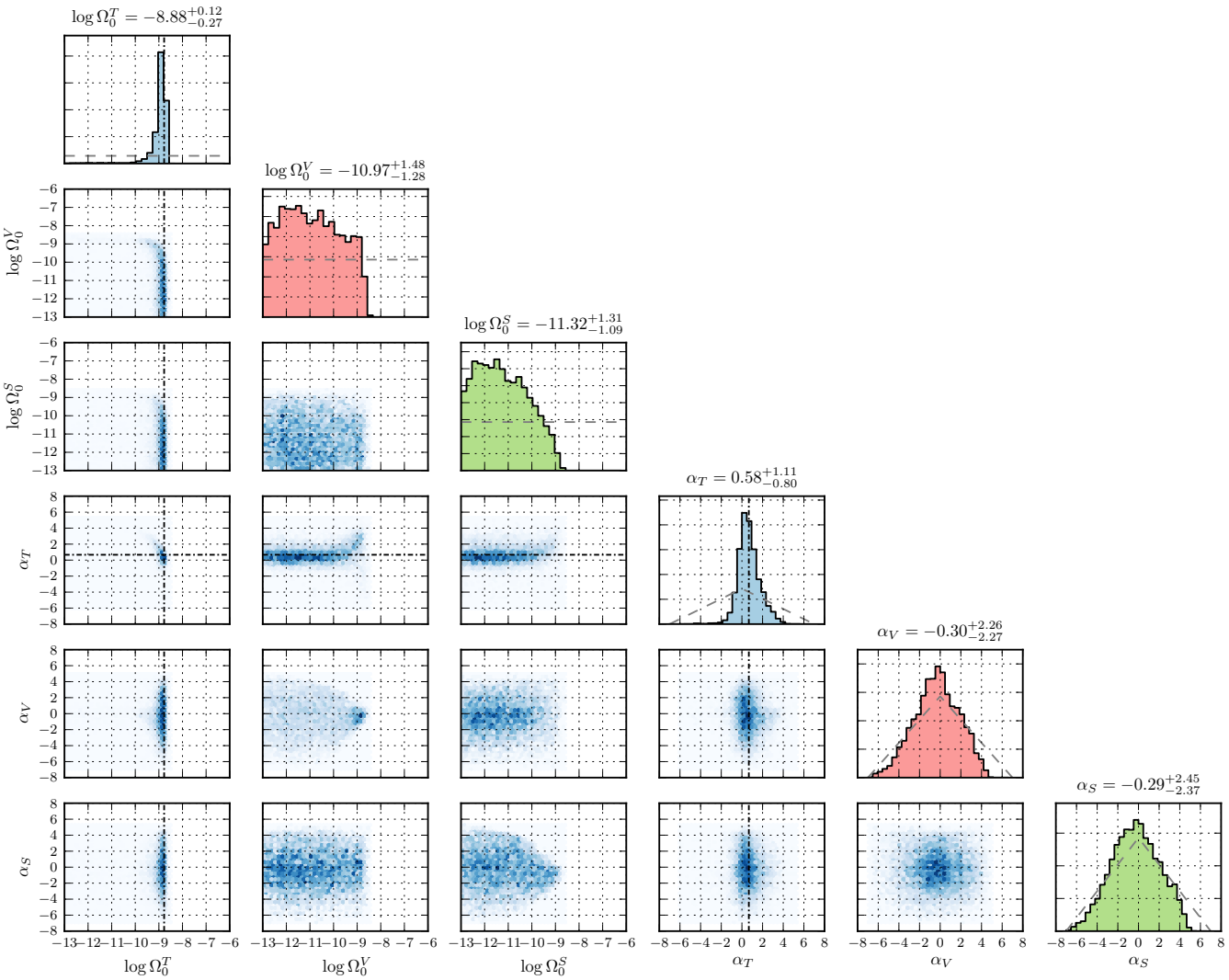

FIG. 12. As in Fig. 10, for a simulated observation of a pure tensor background (Case 2 in Table I). The injected tensor amplitude and slope are indicated by solid black lines. The tensor amplitude and slope posteriors are peaked about their true values. The vector and scalar amplitude posteriors, meanwhile, are consistent with our lower prior bound.

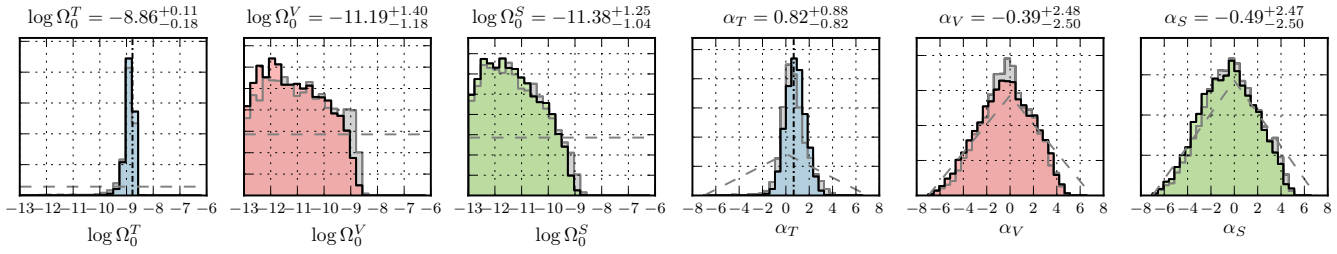

FIG. 13. Marginalized amplitude and slope posteriors for the tensor background observation in Fig. 12, after the additional inclusion of design-sensitivity Advanced Virgo. For reference, the light grey histograms show the Advanced LIGO-only results from Fig. 12. The joint LIGO-Virgo parameter estimation yields a slightly tighter measurement of Ω_0^T, as well as somewhat improved upper limits on Ω_0^V and Ω_0^S.

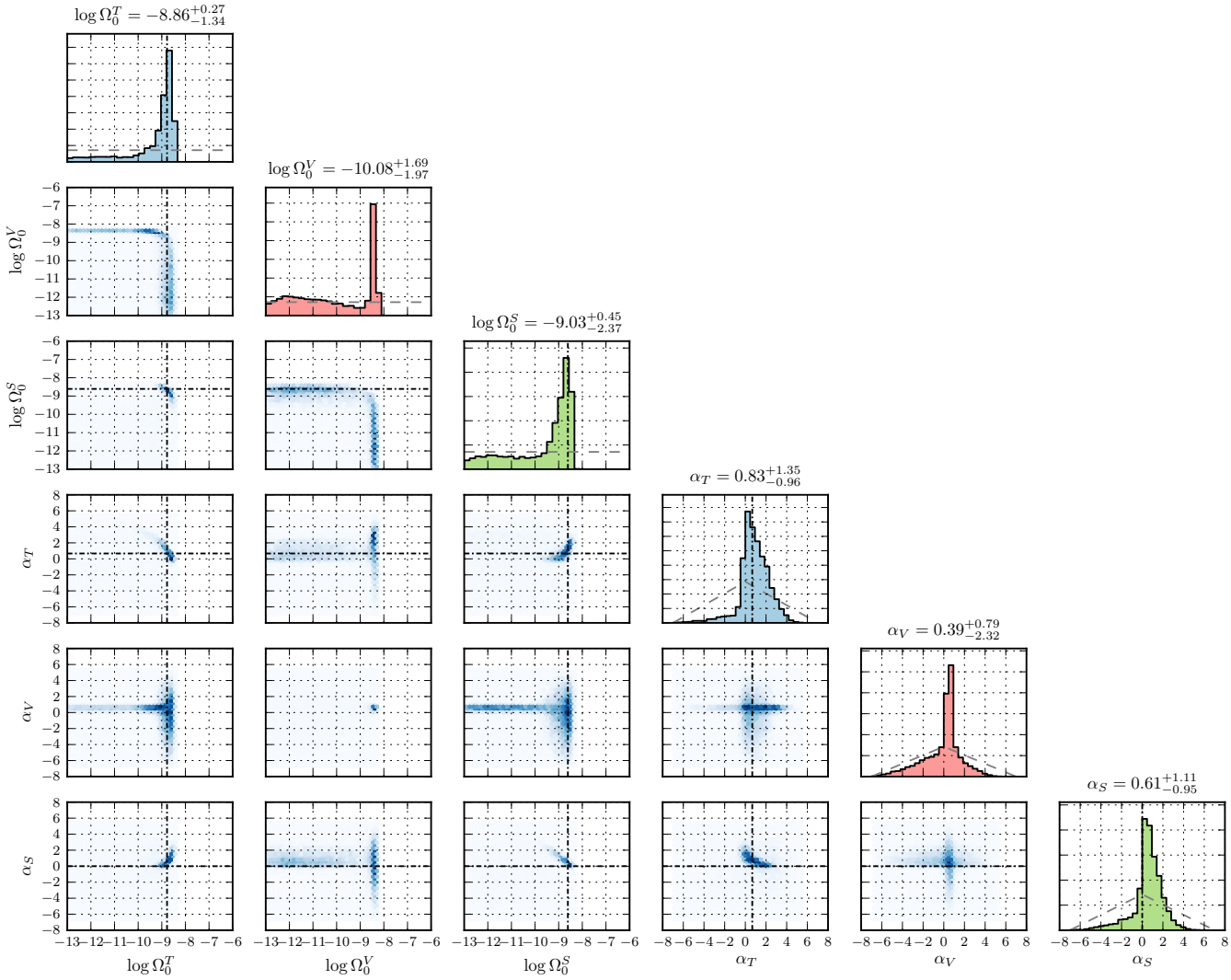

FIG. 14. As in Figs. 10 and 12, for a simulated observation of a mixed tensor and scalar background (Case 3 in Table I). While the Ω_0^T and Ω_0^S posteriors are locally peaked about the true values, much of the observed energy is mistaken for vector polarizations. Thus Advanced LIGO alone is unable to break the degeneracy between tensor, vector, and scalar amplitudes.

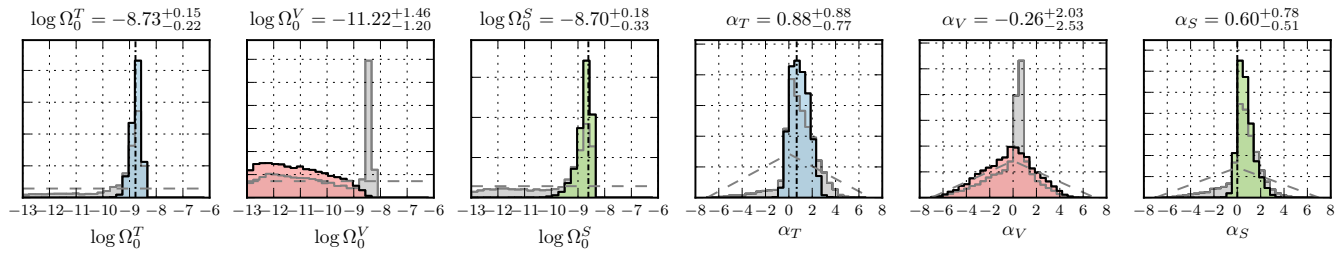

FIG. 15. Marginalized amplitude and slope posteriors for the mixed tensor and scalar background observation in Fig. 14, after the additional inclusion of design-sensitivity Advanced Virgo. For reference, the light grey histograms show the Advanced LIGO-only results from Fig. 14. In contrast to the results in Fig. 14, the observed between polarization modes completely broken when including Advanced Virgo. Thus, while Advanced Virgo does not particularly improve prospects for the detection of a mixed background, it can significantly improve our ability to perform parameter estimation on multiple modes simultaneously.

and scalar ($\log \Omega_0^S = -8.61$ and $\alpha_S = 0$) components. The amplitudes are chosen such that each component is individually observable with $\langle \mathrm{SNR}_{\mathrm{OPT}} \rangle = 5$ after three years of observation. Analysis with `MultiNest` yields odds ratios $\log \mathcal{O}_{\mathrm{N}}^{\mathrm{SIG}} = 38.8$ and $\log \mathcal{O}_{\mathrm{GR}}^{\mathrm{NGR}} = 4.3$, representing a strong detection with some evidence for alternative polarizations.

The posteriors obtained for this data are shown in Fig. 14. Although the tensor and scalar amplitude posteriors are locally peaked about their true values, we see that much of the background's energy is *incorrectly* allocated to vector modes, again illustrating the strong degeneracies that exist between polarizations. This degeneracy is exacerbated for backgrounds with small or negative spectral indices, as in the present case. Such backgrounds preferentially weight low frequencies where the Advanced LIGO overlap reduction functions are all similar (see Fig. 2). Thus, while Advanced LIGO can likely identify the *presence* of alternative polarizations through the odds ratio $\mathcal{O}_{\mathrm{GR}}^{\mathrm{NGR}}$, Advanced LIGO alone is unable to determine which modes (vector or scalar) have been detected.

In contrast, the degeneracies in Fig. 14 are completely broken with the inclusion of Advanced Virgo. Whereas the Ω_0^V posterior is strongly peaked in Fig. 14, we see in Fig. 15 that the posterior is instead entirely consistent with our lower prior bound when including Advanced Virgo. The tensor and scalar amplitude posteriors, meanwhile, are each more strongly-peaked about their correct values and are now inconsistent with the lower amplitude bound. Thus, while Advanced Virgo generally does not generally improve our ability to *detect* a stochastic background, we see that it can significantly improve prospects for simultaneous parameter estimation of multiple polarizations.

VI. BROKEN TENSOR SPECTRA

The stochastic search presented here offers a means to search for alternative gravitational-wave polarizations in a nearly model-independent way. Unlike direct searches for compact binary coalescences, our search makes minimal assumptions about the source and nature of the stochastic background. We do, however, make one notable assumption: that the energy density spectra $\Omega^a(f)$ are well-described by power laws in the Advanced LIGO frequency band. This is expected to be a reasonable approximation for most predicted astrophysical sources of gravitational waves. The backgrounds expected from stellar-mass binary black holes [57], core-collapse supernovae [32], and rotating neutron stars [68–70], for instance, are all well-modelled by power laws in the Advanced LIGO band. It may be, however, that the stochastic background is in fact *not* well-described by a single power law. This may be the case if, for instance, the background is dominated by high-mass binary black holes, an excess of systems at high redshift, or previously-unexpected sources of gravitational waves [57].

Given that our search allows only for power-law background models, how would we interpret a non-power-law background? In particular, if the stochastic background is purely tensorial (obeying general relativity) but is not well-described by a power-law, would our search mistakenly claim evidence for alternative polarizations?

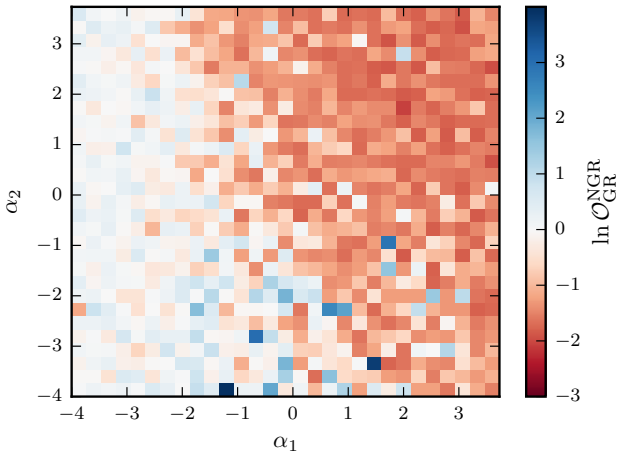

FIG. 16. Odds ratios $\mathcal{O}_{\mathrm{GR}}^{\mathrm{NGR}}$ obtained for simulated Advanced LIGO observations of tensor-polarized broken power law backgrounds with energy density spectra given by Eq. (12). The parameters α_1 and α_2 are the backgrounds' slopes below and above the "knee" frequency f_k, which we take to be 30 Hz (in the center of the stochastic sensitivity band). We scale the amplitude Ω_0 of each background such that it is optimally detectable with $\langle \mathrm{SNR}_{\mathrm{OPT}} \rangle = 5$ after the simulated observation period. By design, these backgrounds are not well-described by single power laws, the form explicitly assumed in our search. Despite this fact, we find that these backgrounds are *not* systematically misclassified as containing vector or scalar polarization.

To investigate this question, we consider simulated Advanced LIGO observations of pure tensor backgrounds described by broken power laws:

$$\Omega^T(f) = \begin{cases} \Omega_0 \left(\frac{f}{f_k}\right)^{\alpha_1} & (f < f_k) \\ \Omega_0 \left(\frac{f}{f_k}\right)^{\alpha_2} & (f \geq f_k). \end{cases} \tag{12}$$

Here, Ω_0 is the background's amplitude at the "knee frequency" f_k, while α_1 and α_2 are the slopes below and above the knee frequency, respectively. We will set the knee frequency to $f_k = 30\,\mathrm{Hz}$, placing the backgrounds' knees in the most sensitive band of the stochastic search. The odds ratios $\mathcal{O}_{\mathrm{GR}}^{\mathrm{NGR}}$ we obtain for these broken power laws are shown in Fig. 16 as a function of the two slopes α_1 and α_2. Each simulation assumes three years of observation at design-sensitivity, and the amplitudes Ω_0 are scaled such that each background has expected $\langle \mathrm{SNR}_{\mathrm{OPT}} \rangle = 5$ after this time. Any trends in Fig. 16 are therefore due to the backgrounds' spectral shapes rather than their amplitudes.

If tensor broken power laws are indeed misclassified by our search, we should expect large, positive $\ln \mathcal{O}_{\mathrm{GR}}^{\mathrm{NGR}}$ values in Fig. 16. Instead, we see that broken power laws are *not* systematically misclassified. When α_1 and α_2 are each positive, we recover $\ln \mathcal{O}_{\mathrm{GR}}^{\mathrm{NGR}} \approx -1.5$, correctly classifying backgrounds as tensorial despite the fact that they are not described by power laws. When $\alpha_1 < 0$, meanwhile, we recover odds ratios scat-

tered about $\ln \mathcal{O}^{\rm NGR}_{\rm GR} \approx 0$. This simply reflects the fact that when α_1 is negative the majority of a background's SNR is collected at low frequencies where Advanced LIGO's tensor, vector, and scalar overlap reduction functions are degenerate. In such a case we do not show preference for either model over the other. Note that we find $\ln \mathcal{O}^{\rm NGR}_{\rm GR} \approx 0$ even along the line $\alpha_2 = \alpha_1$ (for $\alpha_1 < 0$), where the background *is* described by a single power law.

We expect broken power laws to be most problematic when $\alpha_1 > 0$ and $\alpha_2 < 0$; in this case a background's SNR is dominated by a small frequency band around the knee itself. This would be the case if, for instance, the stochastic background were dominated by unexpectedly massive binary black hole mergers [57]. Figure 16 does suggest a larger scatter in $\log \mathcal{O}^{\rm NGR}_{\rm GR}$ for such backgrounds. Even in this region, however, there is not a systematic bias towards larger values of $\mathcal{O}^{\rm NGR}_{\rm GR}$, and the largest recovered odds ratios have $\log \mathcal{O}^{\rm NGR}_{\rm GR} \lesssim 2.5$, well below the level required to confidently claim evidence for the presence of alternative polarizations.

Despite the fact that we assume purely power-law models for the stochastic energy-density spectra, our search appears reasonably robust against broken power law spectra that are otherwise purely tensor-polarized. In particular, in order to be mistakenly classified by our search, a tensor stochastic background would have to emulate the pattern of positive and negative cross-power associated with the vector and/or scalar overlap reduction functions (see, for instance, Fig. 5). This is simply not easy to do without a pathological background. While we have demonstrated this only for Advanced LIGO, we find similarly robust results for three-detector Advanced LIGO-Virgo observations.

Nevertheless, when interpreting odds ratios $\mathcal{O}^{\rm NGR}_{\rm GR}$ it should be kept in mind that the true stochastic background may deviate from a power law. Even if a broken tensor background is not misclassified in our analysis, the *parameter estimation* results we obtain would likely be incorrect (another example of so-called "stealth bias"). It should be pointed out, though, that our analysis is not fundamentally restricted to power-law models. While we adopt power-law models here for computational simplicity, our analysis can be straightforwardly expanded in the future to include more complex models for the stochastic energy-density spectrum.

VII. DISCUSSION

The first direct detection of gravitational waves by Advanced LIGO has opened up new and unique prospects for testing general relativity. One such avenue is the search for vector and scalar gravitational-wave polarizations, predicted by some alternative theories of gravity but prohibited by general relativity. Observation of vector or scalar polarizations in the stochastic background would therefore represent a clear violation of general relativity. The current generation of ground-based detectors, however, is unable to measure the polarization of transient gravitational-wave signals. Instead, searches for long-duration sources like the stochastic background offer the most promising means of directly measuring gravitational-wave polarizations.

In this paper, we explored the procedure by which Advanced LIGO would detect or constrain the presence of vector and scalar polarizations in the stochastic background. In Sect. III, we found that a stochastic background dominated by alternative polarization modes is unlikely to be detected with current search methods optimized only for tensor polarizations. In particular, backgrounds of vector and scalar polarizations may take up to ten times as long to detect with current methods, relative to a search optimized for alternative polarizations. In Sect. IV, we therefore proposed a Bayesian method with which to detect a generically-polarized stochastic background. This method relies on the construction of two odds ratios (see Appendix C). The first serves to determine if a stochastic background has been detected, while the second quantifies evidence for the presence of alternative polarizations in the background. This search has the advantage of being entirely generic; it is capable of detecting and identifying stochastic backgrounds containing any combination of gravitational-wave polarizations. With this method, we demonstrated flat scalar-polarized backgrounds of amplitude $\Omega^S_0 \approx 2 \times 10^{-9}$ can be identified as non-tensorial with Advanced LIGO.

In Sect. V, we then considered the ability of Advanced LIGO to perform simultaneous parameter estimation on tensor, vector, and scalar components of the stochastic background. After three years of observation at design sensitivity, Advanced LIGO will be able to limit the amplitudes of tensor, vector, and scalar polarizations to $\Omega^T_0 < 10^{-10}$, $\Omega^V_0 < 2 \times 10^{-10}$, and $\Omega^S_0 < 1.6 \times 10^{-10}$, respectively, at 95% credibility. If, however, a stochastic background of mixed polarization is detected, Advanced LIGO alone cannot precisely determine the parameters of the tensor, vector, and/or scalar components simultaneously due to large degeneracies between modes.

We also considered how the expected addition of Advanced Virgo to the Hanford-Livingston network will affect the search for alternative polarizations. In Sect. IV, we found that addition of Advanced Virgo does not particularly increase our ability to detect or identify backgrounds of alternative polarizations. However, we found in Sect.V that Advanced Virgo *does* significantly improve our ability to perform parameter estimation on power-law backgrounds, breaking the degeneracies that plagued the Hanford-Livingston analysis.

Relative to other modeled searches for gravitational waves, the stochastic search described here has the advantage of being nearly model-independent. We have, however, made one large assumption: that the tensor, vector, and scalar energy-density spectra are well-described by power laws in the Advanced LIGO band. Finally, in Sect. VI we explored the implications of this assumption, asking the question: would tensor backgrounds *not* described by power laws be mistaken for alternative polarizations in our search? We found that our proposed Bayesian method is reasonably robust against this possibility. In particular, even pure tensor backgrounds with sharply-broken power law spectra are not systematically misidentified by our search.

The non-detection of alternative polarizations in the

stochastic background may yield interesting experimental constraints on extended theories of gravity. In Appendix E, for instance, we demonstrated that an upper limit placed on the scalar background can be leveraged to limit the parameters of scalar-tensor theories of gravity. Although our analysis in Appendix E was limited only to the consideration of binary black holes, there may well exist other interesting or novel constraints obtainable through (non)-observation of alternative modes in the stochastic background.

Meanwhile, any experimental evidence *for* alternative polarizations in the stochastic background would be a remarkable step forward for experimental tests of gravity. Of course, if future stochastic searches do yield evidence for alternative polarizations, careful study would be required to verify that this result is not due to unmodeled effects like non-Gaussianity or anisotropy [20, 71] in the stochastic background. Comparison to polarization measurements of other long-lived sources like rotating neutron stars [25, 26] will additionally aid in the interpretation of stochastic search results.

Several future developments may further improve the ability of ground-based detectors to detect alternative polarization modes in the stochastic background. First, the continued expansion of the ground-based detector network will improve our ability to both resolve the stochastic background and accurately determine its polarization content. Secondly, while we presently assume that the stochastic background is Gaussian, the background contribution from binary black holes is expected to be highly non-Gaussian [19]. Future stochastic searches may therefore be aided by the development of novel data analysis techniques optimized for non-Gaussian backgrounds [72–74].

Acknowledgments

We would like to thank Thomas Dent, Gregg Harry, Joe Romano, and Alan Weinstein for their careful reading of this manuscript, as well as many members of the LIGO-Virgo Collaboration Stochastic Backgrounds working group for helpful comments and conversation. T. C. and M. I. are members of the LIGO Laboratory, supported by funding from the U. S. National Science Foundation. LIGO was constructed by the California Institute of Technology and Massachusetts Institute of Technology with funding from the National Science Foundation and operates under cooperative agreement PHY-0757058. The work of A.M. was supported in part by the NSF grant PHY-1204944 at the University of Minnesota. M.S. is partially supported by STFC (UK) under the research grant ST/L000326/1. E.T. is supported through ARC FT150100281 and CE170100004. This paper carries the LIGO Document Number LIGO-P1700059 and King's College London report number KCL-PH-TH/2017-25.

A. OVERLAP REDUCTION FUNCTIONS

The sensitivity of a two-detector network to a stochastic gravitational-wave background is quantified by the overlap reduction function [54, 55]

$$\gamma(f) \propto \sum_A \int e^{2\pi i f \hat{\mathbf{\Omega}}\cdot\Delta\mathbf{x}/c} F_1^A(\hat{\mathbf{\Omega}}) F_2^A(\hat{\mathbf{\Omega}}) d\mathbf{\Omega}, \tag{A1}$$

where $\Delta\mathbf{x}$ is the displacement vector between detectors, c is the speed of light, and $F^A_{1/2}(\hat{\mathbf{\Omega}})$ are the antenna patterns describing the response of each detector to gravitational-waves of polarization A propagating from the direction $\hat{\mathbf{\Omega}}$. The overlap reduction function is effectively the sky-averaged product of the two detectors' antenna patterns, weighted by the additional phase accumulated as a gravitational wave propagates from one site to the other. It is conventionally normalized such that $\gamma(f) = 1$ for coincident, co-aligned detectors; detectors that are rotated or separated relative to one another have $\gamma(f) < 1$.

In the standard stochastic search, the summation in Eq. (A1) is taken over the tensor plus and cross polarizations. When extending the stochastic search to generic gravitational-wave polarizations, we now must consider three separate overlap reduction functions for the tensor, vector, and scalar modes [22]:

$$\begin{aligned}
\gamma_T(f) &= \frac{5}{8\pi} \sum_{A=\{+,\times\}} \int e^{2\pi i f \hat{\mathbf{\Omega}}\cdot\Delta\mathbf{x}/c} F_1^A(\hat{\mathbf{\Omega}}) F_2^A(\hat{\mathbf{\Omega}}) d\mathbf{\Omega}, \\
\gamma_V(f) &= \frac{5}{8\pi} \sum_{A=\{x,y\}} \int e^{2\pi i f \hat{\mathbf{\Omega}}\cdot\Delta\mathbf{x}/c} F_1^A(\hat{\mathbf{\Omega}}) F_2^A(\hat{\mathbf{\Omega}}) d\mathbf{\Omega}, \\
\gamma_S(f) &= \frac{5}{4\pi} \sum_{A=\{b,l\}} \int e^{2\pi i f \hat{\mathbf{\Omega}}\cdot\Delta\mathbf{x}/c} F_1^A(\hat{\mathbf{\Omega}}) F_2^A(\hat{\mathbf{\Omega}}) d\mathbf{\Omega}.
\end{aligned} \tag{A2}$$

While each overlap reduction function may be calculated numerically via Eq. (A2), they may also be analytically expanded in terms of spherical Bessel functions [22, 54]. See Ref. [22] for definitions of the tensor, vector, and scalar overlap reduction functions in this analytic form.

B. OPTIMAL SIGNAL-TO-NOISE RATIO

Searches for the stochastic background rely on measurements $\hat{Y}(f)$ of the cross-power between two detectors. As discussed in Sect. III, the expectation value and variance of $\hat{Y}(f)$ are given by Eqs. (4) and (5), respectively. Here, we derive the optimal broadband signal-to-noise ratio [Eq. (8)], which combines a spectrum of cross-correlation measurements into a single detection statistic.

Given a measured spectrum $\hat{Y}(f)$ and associated uncertainties $\sigma^2(f)$, a single broadband statistic may be formed via the weighted sum

$$\hat{Y} = \frac{\sum_f \hat{Y}(f) w(f)/\sigma^2(f)}{\sum_f w(f)/\sigma^2(f)}, \tag{B1}$$

where $w(f)$ is a set of yet-undefined weights. The mean and variance of $\hat{Y}$ are

$$\langle \hat{Y} \rangle = \frac{\sum_f \gamma_a(f) \Omega^a(f) w(f)/\sigma^2(f)}{\sum_f w(f)/\sigma^2(f)}, \tag{B2}$$

and

$$\sigma^2 = \frac{\sum_f w^2(f)/\sigma^2(f)}{\left(\sum_f w(f)/\sigma^2(f)\right)^2}, \tag{B3}$$

where $\gamma_a(f)\Omega^a(f)$ denotes summation $\sum_{a\in\{T,V,S\}} \gamma_a(f)\Omega^a(f)$ over polarization modes.

We define a broadband signal-to-noise ratio by SNR $= \hat{Y}/\sigma$. In the limit $df \to 0$, this quantity may be written

$$\text{SNR} = \frac{\left(\hat{Y} \,|\, w\right)}{\sqrt{(w \,|\, w)}}, \tag{B4}$$

where we have substituted Eq. (5) for $\sigma^2(f)$ and made use of the inner product defined in Eq. (7). The expected SNR is maximized when the chosen weights are equal to the true background, such that $w(f) = \gamma_a(f)\Omega^a_{\rm GW}(f)$. In this case, the optimal expected SNR of the stochastic background becomes

$$\langle \text{SNR}_{\rm opt} \rangle = \sqrt{(\gamma_a \Omega^a_{\rm GW} \,|\, \gamma_b \Omega^b_{\rm GW})}. \tag{B5}$$

C. ODDS RATIO CONSTRUCTION

Here, we describe the construction of the odds ratios $\mathcal{O}^{\rm SIG}_{\rm N}$ and $\mathcal{O}^{\rm NGR}_{\rm GR}$ introduced in Sect. IV. Given data $\hat{Y}(f)$, the Bayesian evidence for some hypothesis $\mathcal{A}$ with parameters θ_A is defined

$$P(\hat{Y}|\mathcal{A}) = \int \mathcal{L}(\hat{Y}|\theta_A, \mathcal{A})\pi(\theta_A|\mathcal{A})d\theta_A. \tag{C1}$$

Here, the likelihood $\mathcal{L}(\hat{Y}|\theta_A, \mathcal{A})$ gives the conditional probability of the measured data under hypothesis $\mathcal{A}$ for fixed parameter values, while $\pi(\theta_A|\mathcal{A})$ is the prior probability set on these parameters. When selecting between two such hypotheses $\mathcal{A}$ and $\mathcal{B}$, we may define an odds ratio

$$\mathcal{O}^{\mathcal{A}}_{\mathcal{B}} = \frac{P(\hat{Y}|\mathcal{A})}{P(\hat{Y}|\mathcal{B})}\frac{\pi(\mathcal{A})}{\pi(\mathcal{B})}. \tag{C2}$$

The first factor in Eq. (C2), called the Bayes factor, is the ratio between the Bayesian evidences for hypotheses $\mathcal{A}$ and $\mathcal{B}$. The second term, meanwhile, is the ratio between the prior probabilities $\pi(\mathcal{A})$ and $\pi(\mathcal{B})$ assigned to each hypothesis.

To construct odds ratios for our stochastic background analysis, we will first need the likelihood $\mathcal{L}(\{\hat{Y}\}|\theta, \mathcal{A})$ of a measured cross-correlation spectrum under model $\mathcal{A}$ with parameters θ. In the presence of Gaussian noise, the likelihood of a single measurement $\hat{Y}(f)$ is [54, 57, 75]

$$\mathcal{L}\left(\hat{Y}(f)|\theta, \mathcal{A}\right) \propto \exp\left(-\frac{\left[\hat{Y}(f) - \gamma_a(f)\Omega^a_{\mathcal{A}}(\theta; f)\right]^2}{2\sigma^2(f)}\right), \tag{C3}$$

with variance $\sigma^2(f)$ given by Eq. (5). Here, $\Omega^a_{\mathcal{A}}(\theta; f)$ is the energy-density model corresponding to hypothesis $\mathcal{A}$, evaluated at the given frequency f. The full likelihood $\mathcal{L}(\{\hat{Y}\}|\theta, \mathcal{A})$ for a spectrum of cross-correlation measurements is the product of the individual likelihoods in each frequency bin:

$$\begin{aligned}\mathcal{L}(\{\hat{Y}\}|\theta, \mathcal{A}) &\propto \prod_f \mathcal{L}(\hat{Y}(f)|\theta, \mathcal{A}) \\ &= \mathcal{N}\exp\left[-\frac{1}{2}\left(\hat{Y} - \gamma_a\Omega^a_{\mathcal{A}} \,|\, \hat{Y} - \gamma_b\Omega^b_{\mathcal{A}}\right)\right],\end{aligned} \tag{C4}$$

where $\mathcal{N}$ is a normalization coefficient and we have used the inner product defined by Eq. (7).

As discussed in Sect. IV, we will seek to detect and characterize a generic stochastic background via the construction of two odds ratios: $\mathcal{O}^{\rm SIG}_{\rm N}$, which indicates whether a background of any polarization is present, and $\mathcal{O}^{\rm NGR}_{\rm GR}$, which quantifies evidence for the presence of alternative polarization modes. First consider $\mathcal{O}^{\rm SIG}_{\rm N}$. Under the noise hypothesis (N), we assume that no signal is present [such that $\Omega^a_N(f) = 0$]. From Eq. (C4), the corresponding likelihood is simply

$$\mathcal{L}(\{\hat{Y}\}|\text{N}) = \mathcal{N}\exp\left[-\frac{1}{2}\left(\hat{Y} \,|\, \hat{Y}\right)\right]. \tag{C5}$$

The signal hypothesis (SIG) is somewhat more complex. The signal hypothesis is ultimately the union of seven distinct sub-hypotheses that together describe all possible combinations of tensor, vector, and scalar polarizations [26, 76]. To understand this, first define a "TVS" hypothesis that allows for the simultaneous presence of tensor, vector, and scalar polarization. In this case, we will model the stochastic energy-density spectrum as a sum of three power laws

$$\Omega_{\rm TVS}(f) = \Omega^T_0\left(\frac{f}{f_0}\right)^{\alpha_T} + \Omega^V_0\left(\frac{f}{f_0}\right)^{\alpha_V} + \Omega^S_0\left(\frac{f}{f_0}\right)^{\alpha_S}, \tag{C6}$$

with free parameters Ω^a_0 and α_a setting the amplitude and spectral index of each polarization sector. The priors on these parameters are given by Eqs. (C11) and (C14) below.

In defining the TVS hypothesis, we have made the explicit assumption that tensor, vector, and scalar radiation are each present. This is not the only possibility, of course. A second distinct hypothesis, for instance, is that only tensor and vector polarizations exist. This is our "TV" hypothesis. We model the corresponding energy spectrum as

$$\Omega_{\rm TV}(f) = \Omega^T_0\left(\frac{f}{f_0}\right)^{\alpha_T} + \Omega^V_0\left(\frac{f}{f_0}\right)^{\alpha_V}. \tag{C7}$$

In a similar fashion, we must ultimately define seven such hypotheses, denoted TVS, TV, TS, VS, T, V, and S, to encompass all combinations of tensor, vector, and scalar gravitational-wave backgrounds. Our complete signal hypothesis is given by the union of these seven sub-hypotheses [26, 76]. For each signal sub-hypothesis, we adopt the log-amplitude and slope priors given below in Eqs. (C11) and (C14).

Each of the signal sub-hypotheses are logically independent [26, 76], and so the odds ratio $\mathcal{O}^{\rm SIG}_{\rm N}$ between signal and noise

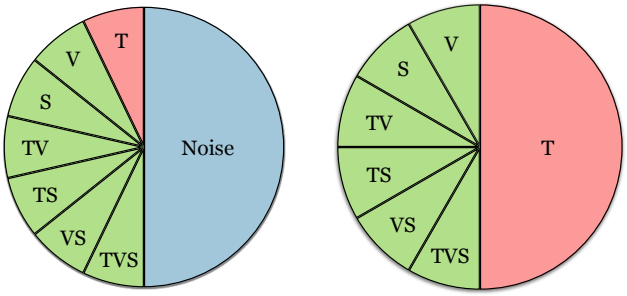

FIG. 17. Illustration of the prior odds assigned to models and sub-hypotheses in the hierarchical Bayesian search for non-GR stochastic backgrounds. When constructing $\mathcal{O}^{\rm SIG}_{\rm N}$, we assign equal prior probability to the noise and signal models, as well as equal probability to the seven signal sub-hypotheses $\{{\rm T},...,{\rm TVS}\}$. Similarly, when constructing $\mathcal{O}^{\rm NGR}_{\rm GR}$, we give equal probability to the non-GR and GR models and identically weight the six non-GR sub-hypotheses $\{{\rm V},...,{\rm TVS}\}$.

hypotheses is given by the sum of odds ratios between the noise hypothesis and each of the seven signal sub-hypotheses:

$$\mathcal{O}^{\rm SIG}_{\rm N} = \sum_{\mathcal{A}\in\{{\rm T,V,S,...}\}} \mathcal{O}^{\mathcal{A}}_{\rm N}. \tag{C8}$$

As illustrated in Fig. 17, we assign equal prior probability to the signal and noise hypotheses. Within the signal hypothesis, we weight each of the signal sub-hypotheses equally, such that the prior odds between e.g. the T and N hypothesis is $\pi({\rm T})/\pi({\rm N}) = 1/7$. We note that our choice of prior probabilities is not unique; there may exist other valid choices as well. Our analysis can easily accommodate different choices of prior weight.

The odds ratio $\mathcal{O}^{\rm NGR}_{\rm GR}$ is constructed similarly. In this case, we are selecting between the hypothesis that the stochastic background is purely tensor-polarized (GR), or the hypothesis that additional polarization modes are present (NGR). The GR hypothesis is identical to our tensor-only hypothesis T from above:

$$\Omega_{\rm GR}(f) = \Omega_0^T \left(\frac{f}{f_0}\right)^{\alpha_T}. \tag{C9}$$

The NGR hypothesis, on the other hand, will be the union of the six signal sub-hypotheses that are inconsistent with general relativity: V, S, TV, TS, VS, and TVS. The complete odds ratio between NGR and GR hypothesis is then

$$\mathcal{O}^{\rm NGR}_{\rm GR} = \sum_{\mathcal{A}\in\{{\rm V,S,TV,...}\}} \mathcal{O}^{\mathcal{A}}_{\rm T}. \tag{C10}$$

As shown in Fig. 17, we have assigned equal priors to the GR and NGR hypotheses as well as identical priors to the six NGR sub-hypotheses.

In computing the odds ratios $\mathcal{O}^{\rm SIG}_{\rm N}$ and $\mathcal{O}^{\rm NGR}_{\rm GR}$, we also need priors for the various parameters governing each model for the stochastic background. In the various energy-density models presented above, we have defined two classes of parameters: amplitudes Ω_0^a and spectral indices α_a of the background's various polarization components. For each amplitude parameter, we will use the prior

$$\pi(\Omega_0) \propto \begin{cases} 1/\Omega_0 & (\Omega_{\rm Min} \leq \Omega_0 \leq \Omega_{\rm Max}) \\ 0 & ({\rm Otherwise}) \end{cases}. \tag{C11}$$

This corresponds to a uniform prior in the log-amplitudes between $\log\Omega_{\rm Min}$ and $\log\Omega_{\rm Max}$. To generate the results in this paper, we use the limits $\Omega_{\rm Min} = 10^{-13}$ and $\Omega_{\rm Max} = 10^{-6}$, consistent with upper limits placed by Initial LIGO and Virgo [58].

To obtain priors on α, we use the fact that the spectral index may be written as

$$\alpha = \frac{\log\left(\Omega_1/\Omega_0\right)}{\log\left(f_1/f_0\right)}, \tag{C12}$$

where Ω_0 and Ω_1 are the amplitudes of the background at two different frequencies f_0 and f_1. Given priors $\pi_0(\log\Omega_0)$ and $\pi_1(\log\Omega_1)$ on the amplitudes, the corresponding prior on α is found through the convolution

$$\pi(\alpha) = \int \pi_1(\log\Omega_1)\pi_0(\log\Omega_1 - \alpha\log(f_1/f_0))d\log\Omega_1. \tag{C13}$$

If we choose a prior $\pi_1(\log\Omega_1)$ identical to the uniform prior on $\log\Omega_0$ and, for convenience, set $f_1 = 10f_0$ (such that $\log(f_1/f_0) = 1$), then the resulting prior on α is

$$\pi(\alpha) = \begin{cases} \frac{1}{\alpha_{\rm Max}}\left(1 - \frac{|\alpha|}{\alpha_{\rm Max}}\right) & (|\alpha| \leq \alpha_{\rm Max}) \\ 0 & ({\rm Otherwise}), \end{cases} \tag{C14}$$

where $\alpha_{\rm Max} = \log(\Omega_{\rm Max}/\Omega_{\rm Min})$. This prior is triangular in shape, preferentially weighting shallower energy-density spectra.

In Sects. IV and V, we additionally considered the performance of the three-detector Advanced LIGO-Virgo network. The Bayesian framework considered here is easily extended to accommodate multiple detector pairs. Specifically, multiple detector pairs are included by modifying the likelihood Eq. (C4) used to evaluate the Bayesian evidences for each hypothesis. The three LIGO and Virgo detectors allow for the measurement of three cross-correlation spectra: $\hat{Y}^{\rm HL}(f)$, $\hat{Y}^{\rm HV}(f)$, and $\hat{Y}^{\rm LV}(f)$. Assuming that each baseline is independent, the joint likelihood for the three sets of measurements factorizes:

$$\begin{aligned}
&\mathcal{L}(\{\hat{Y}^{\rm HL},\hat{Y}^{\rm HV},\hat{Y}^{\rm LV}\}|\theta,\mathcal{A}) \\
&\quad= \mathcal{L}(\{\hat{Y}^{\rm HL}\}|\theta,\mathcal{A})\,\mathcal{L}(\{\hat{Y}^{\rm HV}\}|\theta,\mathcal{A})\,\mathcal{L}(\{\hat{Y}^{\rm LV}\}|\theta,\mathcal{A}) \\
&\quad= \mathcal{N}\exp\Big\{-\frac{1}{2}\Big[\left(\hat{Y}^{\rm HL} - \gamma_a^{\rm HL}\Omega^a_{\mathcal{A}}\,|\,\hat{Y}^{\rm HL} - \gamma_b^{\rm HL}\Omega^b_{\mathcal{A}}\right) \\
&\qquad\qquad + \left(\hat{Y}^{\rm HV} - \gamma_a^{\rm HV}\Omega^a_{\mathcal{A}}\,|\,\hat{Y}^{\rm HV} - \gamma_b^{\rm HV}\Omega^b_{\mathcal{A}}\right) \\
&\qquad\qquad + \left(\hat{Y}^{\rm LV} - \gamma_a^{\rm LV}\Omega^a_{\mathcal{A}}\,|\,\hat{Y}^{\rm LV} - \gamma_b^{\rm LV}\Omega^b_{\mathcal{A}}\right)\Big]\Big\},
\end{aligned} \tag{C15}$$

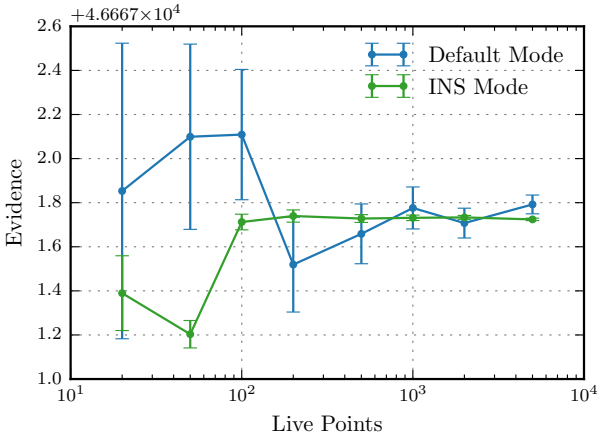

FIG. 18. `MultiNest` Bayesian evidences for a single simulated SGWB observation as a function of the number of live points chosen. For the simulated data, we assume a tensor-polarized background (with $\Omega_0^T = 2 \times 10^{-8}$ and $\alpha_T = 2/3$) observed for one year with design-sensitivity Advanced LIGO, and compute evidence using the T model (see Sect. IV). Results are shown for both `MultiNest`'s Default and INS modes; also shown are the error estimates provided by each mode. To compute the results presented in this paper, we used $n = 2000$ live points.

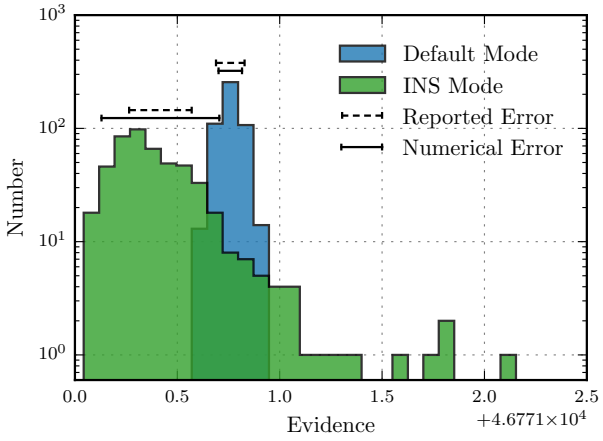

FIG. 19. Histograms of `MultiNest` evidences (for the TVS model; see Sect. IV) obtained by evaluating a single simulated data set 500 times in both the Default and INS modes. To generate the simulated data, we assume a one-year observation of a tensor background ($\Omega_0^T = 2 \times 10^{-8}$ and $\alpha_T = 2/3$) with design-sensitivity Advanced LIGO. The dashed error bars show the mean 68% confidence interval reported by each method, while the solid error bars show the true 68% confidence interval computed from the evidence distributions.

where we have explicitly distinguished between the overlap reduction functions for each baseline and $\mathcal{N}$ is again a normalization constant. Other than the above change to the likelihood, all other details of the odds ratio construction is unchanged when including three detectors.

D. EVALUATING BAYESIAN EVIDENCES WITH `MULTINEST`

Here we summarize details associated with using `MultiNest` to evaluate Bayesian evidences for various models of the stochastic background. The `MultiNest` algorithm allows for several user-defined parameters, including the number n of live points used to sample the prior volume and the sampling efficiency ϵ, which governs acceptance rate of new proposed live points (see e.g. Ref. [64] for details). `MultiNest` also provides the option to run in Default or Importance Nested Sampling (INS) modes, each of which use different methods to evaluate evidences [65].

To set the number of live points, we investigated the convergence of `MultiNest`'s evidence estimates with increasing values of n. For a single simulated observation of a tensorial background (with amplitude $\Omega_0^T = 2 \times 10^{-8}$ and slope $\alpha_T = 2/3$), for instance, Fig. 18 shows the recovered evidence for the T hypothesis (see Appendix C above) as a function of n, using both the Default (blue) and INS modes (green). The results are reasonably stable for $n \gtrsim 1000$; we choose $n = 2000$ live points. Meanwhile, our recovered evidence estimates do not exhibit noticeable dependence on the sampling efficiency; we choose the recommended values $\epsilon = 0.3$ for evidence evaluation and $\epsilon = 0.8$ for parameter estimation [64].

In addition to computing Bayesian evidences, `MultiNest` also returns an estimate of the numerical error associated with each evidence calculation. See, for instance, the error bars in Fig. 18. To gauge the accuracy of these error estimates, we construct a single simulated Advanced LIGO observation of a purely-tensorial stochastic background (again with $\Omega_0^T = 2 \times 10^{-8}$ and $\alpha_T = 2/3$). We then use `MultiNest` to compute the corresponding TVS evidence 500 times, in both Default and INS modes. The resulting distributions of evidences are shown in Fig. 19. The dashed error bars show the averaged $\pm 1\sigma$ intervals reported by `MultiNest`, while the solid bars show the $\pm 1\sigma$ intervals obtained manually from the distributions. We see that the errors reported by `MultiNest`'s Default mode appear to accurately reflect the numerical error in the evidence calculation, while the errors reported by the INS mode are underestimated by a factor of ~ 2.

Additionally, Fig. 19 illustrates several systematic differences between the Default and INS results. First, Default mode appears significantly more precise than INS mode, giving rise to a much narrower distribution of evidences. Not only is the INS evidence distribution wider, but it exhibits a large tail extending several units in evidence above the mean. We find that similarly long tails also appear for other pairs of injected signals and recovered models. For this reason, we choose to use `MultiNest`'s Default mode in all evidence calculations. Typical numerical errors in Default mode are of order $\delta(\text{evidence}) \sim 0.1$, and so the uncertainty associated with a log-odds ratio is $\delta(\ln \mathcal{O}) \sim \sqrt{2}\delta(\text{evidence})$, again of

order 0.1. Additionally, we see that the peaks of the Default and INS distributions do not coincide. In general, the peaks of evidence distributions from the Default and INS modes lie ~ 0.3 units apart. Thus there may be additional systematic uncertainties in a given evidence calculation. However, as long as we consistently use one mode or the other (in our case, Default mode), any uniform systematic offset in the evidences will simply cancel when we ultimately compute a log-odds ratio.

E. TESTING SCALAR-TENSOR THEORIES WITH THE BINARY BLACK HOLE BACKGROUND

The stochastic search presented in this paper offers a purely phenomenological means of testing general relativity. In particular, the observation of vector or scalar polarizations in the background would represent a clear violation of general relativity. In addition to this broad test of general relativity, the results of this search may also be able to test and/or constrain specific alternative theories of gravity. Here we show an example of this, demonstrating that observation of the stochastic background from binary black holes can serve to constrain scalar-tensor theories of gravity.

At leading post-Newtonian (PN) order, the total gravitational-wave power dE/dt emitted by a single binary black hole is the sum of the power radiated into both tensor and scalar modes:

$$\frac{dE}{dt} = \frac{dE_T}{dt} + \frac{dE_S}{dt}. \tag{E1}$$

We assume that dE_T/dt is unchanged from the value predicted by general relativity. The scalar modes, meanwhile, are emitted as dipole waves. The power emitted via these scalar dipole waves may be parameterized as [38]

$$\frac{dE_{\rm S}}{dt} = B\left(\frac{c^2 r}{GM}\right)\frac{dE_T}{dt}, \tag{E2}$$

where M is the binary's total mass, r is its orbital separation, and B is a dimensionless parameter which can be predicted by a given scalar-tensor theory. Note that we recover general relativity in the limit $B \to 0$.

There are three frequencies of interest in this system: the orbital frequency $f_{\rm source}$ of the binary, the frequency f_T of the tensor-polarized quadrupole gravitational waves, and the frequency f_S of the scalar-polarized dipole waves. These three frequencies are related via

$$f_{\rm source} = \frac{1}{2} f_T = f_S. \tag{E3}$$

This relationship can be understood by the fact that a dipole moment returns to its initial state after a full rotation by 2π radians, whereas a quadrupole moment returns to its original state after only a rotation by π radians.

Assuming that the rate of the binary's orbital decay $\dot{f}_{\rm source}$ remains approximately unchanged from the rate predicted by general relativity ($B \ll 1$), the scalar energy spectrum is

$$\begin{aligned}\frac{dE_S}{df_S} &= \frac{1}{\dot{f}_S}\frac{dE_S}{dt} \\ &= \frac{Bc^2}{(4\pi^2)^{1/3}}(f_S GM)^{-2/3}\frac{dE_T}{d(f_{\rm T}/2)}.\end{aligned} \tag{E4}$$

This is expected to be a good approximation for the duration of the inspiral before the binary crosses its innermost stable circular orbit.

The stochastic background of scalar gravitational waves arising from all unresolved binary black holes in the Universe is given by [19, 57, 77]

$$\Omega^S_{\rm GW}(f) = \frac{f}{\rho_c}\int_0^{z_{\rm max}} \frac{R_m(z)\frac{dE_S}{df_S}[f(1+z)]}{(1+z)H(z)}{\rm d}z. \tag{E5}$$

The integral is taken over redshift, with $z_{\rm max} = 10$ being the maximum redshift considered. $H(z)$ gives the evolution of the Hubble parameter with redshift in a flat Universe, while $R_m(z)$ gives the binary black hole merger rate per comoving volume at redshift z. Note that, within the integral, the scalar energy spectrum $dE^S_{\rm GW}/df_S$ is evaluated at the source-frame frequency $f(1+z)$.

During the inspiral phase of a binary black hole system, the energy spectrum of its tensor gravitational waves is $dE^T_{\rm GW}/df_{\rm T} \propto f^{-1/3}$ [16]. The energy spectrum of scalar dipole waves, on the other hand, is $dE^S_{\rm GW}/df_{\rm S} \propto f^{-1}$ from Eq. (E4). The predicted tensorial and scalar stochastic backgrounds from binary black holes will therefore have different characteristic slopes. Using Eq. (E5), the energy density of tensor-polarized gravitational waves is expected to scale as

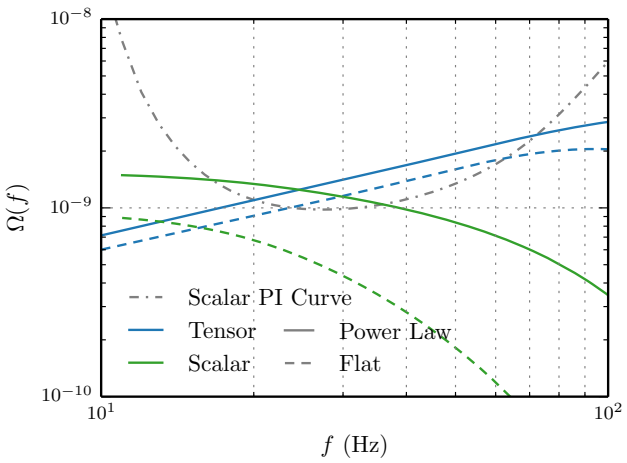

FIG. 20. Example scalar spectra from binary black hole mergers, assuming a relationship of the form Eq. (E2) between radiated tensor and scalar modes. We choose $B = 0.2$ as a fiducial value, and show results assuming two different binary black hole mass distributions; see Ref. [3] for details. At fixed B, we see that the mass distributions with lower median mass allow for a louder scalar background, consistent with the fact that the dipole enhancement is larger for smaller total mass (see Eq. E4).

Mass Distribution	Median chirp mass ($M_\odot$)	Local rate ($\mathrm{Gpc}^{-3}\mathrm{yr}^{-1}$)	Range of 1 σ limits on B
Flat	16	31^{+42}_{-21}	0.14-1.1
Power Law (-2.35)	8.6	97^{+135}_{-67}	0.06-0.46

TABLE II. Best and worst-case 95% confidence limits on B obtainable assuming the "Flat" and "Power Law" binary black hole mass distributions considered in Fig. 20. Also given are the median binary black hole chirp mass and merger rate for each distribution. The uncertainties given on the merger rates correspond to the 90% credible intervals obtained through analysis of Advanced LIGO's O1 observing run [3]. Limits on B are obtained by computing the parameter values at which the scalar energy-density spectra lie tangent to the PI curve, and hence are detectable with $\mathrm{SNR} \gtrsim 2$. The best and worst-case limits are obtained by assuming different values for the local binary black hole merger rate. To find the best-case limits, we adopt merger rates equal to the upper bounds on the 90% credible rate interval (yielding very loud backgrounds). The worst-case limits, meanwhile, are given by the lower bounds on the credible rate intervals.

$\Omega^T_{\mathrm{GW}}(f) \propto f^{2/3}$. Meanwhile, the scalar energy density is expected to be flat at low frequencies, with $\Omega^S_{\mathrm{GW}} \propto f^0$.

As an example, in Fig. 20 we show the scalar spectra $\Omega^S_{\mathrm{GW}}(f)$ corresponding to $B = 0.2$ for two different models for the binary black hole mass distribution: a power-law distribution (solid green) and a flat distribution (dashed green). The blue curves, meanwhile, show the standard tensor-polarized background predicted in case. The two mass distributions considered are described in detail in Refs. [3, 78, 79]. For each model, Table II lists the median binary chirp mass, as well as the median rate of binary black hole mergers as measured in Advanced LIGO's O1 observing run [3]. To compute the energy-density spectra shown in Fig. 20, we have adopted the same merger rate $R_m(z)$ and cosmological parameters as those used in the `Fiducial` model of Refs. [18] and [19]. For reference, in Fig. 20 we additionally show the 2σ scalar PI curve for Advanced LIGO at design sensitivity, assuming three years of integration (see Sect. III) [59].

From Eq. (E4), note that scalar dipole radiation is enhanced for *smaller* total masses. As a result, we see in Fig. 20 that the power law mass distribution (with median chirp mass $8.6\,M_\odot$) yields a scalar spectrum that is a factor of two larger than that of the flat distribution (median chirp mass $16\,M_\odot$). This is much greater than the difference between the tensor spectra in each case.

By comparing the scalar spectra to the PI curve, we can estimate the upper limits that stochastic searches with design-sensitivity Advanced LIGO can place on B. As approximate power laws, scalar spectra that lie tangent to or above the PI curve are detectable with $\mathrm{SNR} \gtrsim 2$ after three years of integration at design sensitivity. Values of B which bring the scalar spectra tangent to the PI curve therefore correspond to the $\sim 95\%$ confidence (2σ) upper limits that can be placed on B, given a null detection of a scalar background. In the final column of Table II, we list the resulting best and worst-case limits on B under each mass distribution. The best-case limits correspond to the loudest possible backgrounds with the highest possible merger rates. For this case we adopt the upper bound on the 90% credible rate interval, as given in Table II, for our local merger rate. The worst-case limits, meanwhile, occur under the weakest possible backgrounds, given by adopting the lower bounds on the 90% credible intervals.

[1] B. P. Abbott *et al.*, Phys. Rev. Lett. **116**, 061102 (2016).
[2] B. P. Abbott *et al.*, Phys. Rev. Lett. **116**, 241103 (2016).
[3] B. P. Abbott *et al.*, Phys. Rev. X **6**, 041015 (2016).
[4] J. Aasi *et al.*, Class. Quantum Gravity **32**, 074001 (2015).
[5] D. M. Eardley, D. L. Lee, A. P. Lightman, R. V. Wagoner, and C. M. Will, Physical Review Letters **30**, 884 (1973).
[6] D. M. Eardley, D. L. Lee, and A. P. Lightman, Phys. Rev. D**8**, 3308 (1973).
[7] J. Gair, M. Vallisneri, S. L. Larson, and J. G. Baker, Living Rev. Rel. **16**, 7 (2013).
[8] C. M. Will, Living Rev. Rel. **17**, 4 (2014).
[9] B. P. Abbott *et al.*, Phys. Rev. Lett. **116**, 221101 (2016).
[10] B. P. Abbott *et al.*, Phys. Rev. D **94**, 064035 (2016).
[11] C. de Rham, J. T. Deskins, A. J. Tolley, and S.-Y. Zhou, (2016), arXiv:1606.08462.
[12] J. D. Romano and N. J. Cornish, Living Rev. Rel. **20**, 2 (2017).
[13] K. Chatziioannou, N. Yunes, and N. Cornish, Phys. Rev. D **86**, 022004 (2012).
[14] P. A. Rosado, Phys. Rev. D **84**, 084004 (2011).
[15] X.-J. Zhu, E. Howell, T. Regimbau, D. Blair, and Z.-H. Zhu, Astrophys. J. **739**, 86 (2011).
[16] C. Wu, V. Mandic, and T. Regimbau, Phys. Rev. D **85**, 104024 (2012).
[17] X.-J. Zhu, E. J. Howell, D. G. Blair, and Z.-H. Zhu, Mon. Not. R. Astron. Soc. **431**, 882 (2013).
[18] B. P. Abbott *et al.*, Phys. Rev. Lett. **118**, 121101 (2017).
[19] B. P. Abbott *et al.*, Phys. Rev. Lett. **116**, 131102 (2016).
[20] B. P. Abbott *et al.*, Phys. Rev. Lett. **118**, 121102 (2017).
[21] E. Berti *et al.*, Classical and Quantum Gravity **32**, 243001 (2015).
[22] A. Nishizawa, A. Taruya, K. Hayama, S. Kawamura, and M.-a. Sakagami, Phys. Rev. D **79**, 082002 (2009).
[23] A. Nishizawa, A. Taruya, and S. Kawamura, Phys. Rev. D **81**, 104043 (2010).
[24] A. Nishizawa and K. Hayama, Phys. Rev. D **88**, 064005 (2013).
[25] M. Isi, A. J. Weinstein, C. Mead, and M. Pitkin, Phys. Rev. D**91**, 082002 (2015).
[26] M. Isi, M. Pitkin, and A. J. Weinstein, arXiv:1703.07530.
[27] C. Brans and R. H. Dicke, Phys. Rev. **124**, 925 (1961).
[28] D. Gerosa, U. Sperhake, and C. D. Ott, Class. Quantum Gravity **33**, 135002 (2016).
[29] S. E. Gossan *et al.*, Phys. Rev. D **93**, 042002 (2016).
[30] B. P. Abbott *et al.*, Phys. Rev. D **94**, 102001 (2016).
[31] S. M. Adams, C. S. Kochanek, J. F. Beacom, M. R. Vagins, and

K. Z. Stanek, Astrophys. J. **778**, 164 (2013).
[32] K. Crocker *et al.*, Phys. Rev. D **92**, 063005 (2015).
[33] K. Crocker *et al.*, Phys. Rev. D. **95**, 063015 (2017).
[34] T. Damour and G. Esposito-Farese, Class. Quantum Gravity **9**, 2093 (1992).
[35] T. Damour and G. Esposito-Farese, Phys. Rev. Lett. **70**, 2220 (1993).
[36] P. C. C. Freire *et al.*, Mon. Not. R. Astron. Soc. **423**, 3328 (2012).
[37] J. Antoniadis *et al.*, Science **340**, 1233232 (2013).
[38] E. Barausse, N. Yunes, and K. Chamberlain, Phys. Rev. Lett. **116**, 241104 (2016).
[39] M. Horbatsch and C. Burgess, J. Cosmol. Astropart. Phys. **2012**, 010 (2012).
[40] E. Berti, V. Cardoso, L. Gualtieri, M. Horbatsch, and U. Sperhake, Phys. Rev. D **87**, 124020 (2013).
[41] T. Damour and A. Vilenkin, Phys. Rev. Lett. **78**, 2288 (1997).
[42] S. Ölmez, V. Mandic, and X. Siemens, Phys. Rev. D **81**, 1 (2010).
[43] M. Maggiore, Phys. Rep. **331**, 283 (2000).
[44] C. Caprini, R. Durrer, and G. Servant, Phys. Rev. D **77**, 124015 (2008).
[45] C. Caprini *et al.*, J. Cosmol. Astropart. Phys. **2016**, 001 (2016).
[46] R. Tso, M. Isi, Y. Chen, and L. Stein, ArXiv e-prints (2016), arXiv:1608.01284.
[47] T. Narikawa *et al.*, Phys. Rev. D**91**, 062007 (2015).
[48] V. A. Kostelecky, Phys. Rev. D **69**, 105009 (2004).
[49] V. A. Kostelecky and M. Mewes, Phys. Lett. B **757**, 510 (2016).
[50] N. Yunes, K. Yagi, and F. Pretorius, Phys. Rev. D **94**, 084002 (2016).
[51] T. Damour, Classical and Quantum Gravity **29**, 184001 (2012).
[52] T. Damour and K. Nordtvedt, Physical Review Letters **70**, 2217 (1993).
[53] A. Joyce, B. Jain, J. Khoury, and M. Trodden, Physics Reports **568**, 1 (2015).
[54] B. Allen and J. D. Romano, Phys. Rev. D **59**, 102001 (1999).
[55] N. Christensen, Phys. Rev. D **46**, 5250 (1992).
[56] G. Cella *et al.*, Classical and Quantum Gravity **24**, S639 (2007).
[57] T. Callister, L. Sammut, S. Qiu, I. Mandel, and E. Thrane, Phys. Rev. X **6**, 031018 (2016).
[58] J. Aasi *et al.*, Phys. Rev. Lett. **113**, 231101 (2014).
[59] E. Thrane and J. D. Romano, Phys. Rev. D **88**, 124032 (2013).
[60] M. Vallisneri and N. Yunes, Phys. Rev. D**87**, 102002 (2013).
[61] S. Vitale and W. Del Pozzo, Phys. Rev. D**89**, 022002 (2014).
[62] J. Buchner *et al.*, Astron. Astrophys. **564**, A125 (2014).
[63] F. Feroz and M. P. Hobson, Mon. Not. R. Astron. Soc. **384**, 449 (2008).
[64] F. Feroz, M. P. Hobson, and M. Bridges, Mon. Not. R. Astron. Soc. **398**, 1601 (2009).
[65] F. Feroz, M. P. Hobson, E. Cameron, and A. N. Pettitt, (2013), arXiv:1306.2144.
[66] J. Skilling, Nested sampling, in *AIP Conf. Proc.* Vol. 735, pp. 395–405, AIP, 2004.
[67] J. Skilling, Bayesian Analysis **1**, 833 (2006).
[68] T. Regimbau and V. Mandic, Class. Quantum Gravity **25**, 184018 (2008).
[69] C.-J. Wu, V. Mandic, and T. Regimbau, Phys. Rev. D **87**, 042002 (2013).
[70] D. Talukder, E. Thrane, S. Bose, and T. Regimbau, Phys. Rev. D **89**, 123008 (2014).
[71] D. Meacher, E. Thrane, and T. Regimbau, Phys. Rev. D **89**, 084063 (2014).
[72] E. Thrane, Phys. Rev. D **87**, 043009 (2013).
[73] L. Martellini and T. Regimbau, Phys. Rev. D **89**, 124009 (2014).
[74] N. J. Cornish and J. D. Romano, Phys. Rev. D **92**, 042001 (2015).
[75] V. Mandic, E. Thrane, S. Giampanis, and T. Regimbau, Phys. Rev. Lett. **109**, 171102 (2012).
[76] T. G. F. Li *et al.*, Phys. Rev. D**85**, 082003 (2012).
[77] E. S. Phinney, (2001), arXiv:astro-ph/0108028.
[78] B. P. Abbott *et al.*, Astrophys. J. **833**, L1 (2016).
[79] B. P. Abbott *et al.*, Astrophys. J. Suppl. Ser. **227**, 14 (2016).